Front. Struct. Civ. Eng. 2025, 19(3): 319–340
https://doi.org/10.1007/s11709-025-1147-x

RESEARCH ARTICLE

Long-term creep behavior of expansive agent core concrete in full-scale concrete-filled steel tube from the world's largest span arch bridge study

Zheng CHEN[a,b], Changjie WU[a,b], Ben CHEN[a,b], Yang YANG[a,b], Weiying LIANG[c], Yunchao TANG[d*], Jielian ZHENG[a,b*]

[a] *School of Civil Engineering and Architecture, State Key Laboratory of Featured Metal Materials and Life-cycle Safety for Composite Structures, Guangxi University, Nanning 530004, China*

[b] *Key Laboratory of Disaster Prevention and Structural Safety of China Ministry of Education, Guangxi University, Nanning 530004, China*

[c] *Guangxi Polytechnic of Construction, Nanning 530007, China*

[d] *Guangdong Provincial Key Laboratory of Intelligent Disaster Prevention and Emergency Technologies for Urban Lifeline Engineering, Dongguan University of Technology, Dongguan 523808, China*

[*] *Corresponding authors. E-mails: joshua0115@gxu.edu.cn; zhengjielian@163.com*

ABSTRACT The Tian'e Longtan Bridge, currently under construction and boasting the world's largest span arch at 600 m, employs a concrete-filled steel tube (CFST) as its primary structural component, forming the stiffness skeleton upon which an outer reinforced concrete arch ring is constructed. As the internal defects of CFST, once encased by outer concrete, cannot be remedied, it becomes imperative to prevent long-term debonding of the core concrete. In recent years, expansion agents have been extensively utilized in CFST arch bridge engineering to compensate for early autogenous and thermal shrinkage. However, a comprehensive comprehension of the creep behavior of core concrete expansion under extended steel tube confinement remains elusive. To address this concern, the radial expansion process of the core concrete can be segmented into two stages: debonding and restriction. We derive a long-term deformation model for the radial expansion of core concrete during the restriction stage, based on elastic mechanics and linear creep mechanics. We represent the expansion process of these two stages uniformly using piecewise functions. Subsequently, in conjunction with the ongoing construction of the Tian'e Longtan Bridge, we measure the core concrete's behavior in full-size CFST specimens (Φ0.92 m × 12 m × 0.01 m) both with and without expansion agents for up to 114 d. This validates the practicality of the creep model and enables us to determine its relevant parameters. Our results reveal that a debonding gap of 0.142 m occurred before the initial setting of the core concrete. The core concrete underwent a radial expansion of 290.1 × 10^{-6}, with 158.3 × 10^{-6} being used to address early debonding, and the remaining 131.8 × 10^{-6} generating self-stress on the steel tube. The creep model indicates that radial creep of the core concrete persisted for approximately six months under the hoop limitation of the steel tube, resulting in a residual expansion deformation of 26.4 × 10^{-6} and a residual self-stress of 0.119 MPa. Additionally, axial deformation results of CFST without expansion agents demonstrated a decreasing constraining force of the steel tube on the core concrete from the outer to the inner sections, attributable to local core concrete yield. Conversely, the inclusion of an expansion agent altered the stress state of the core concrete, maintaining consistent constraining forces within the same section. As a result, we derive an axial long-term expansion model for the core concrete under steel tube restriction. Finally, the introduction of laboratory specimen deformations enhances the practicality of our model, with results demonstrating strong alignment between measured data and the model. The experimental findings and theoretical models developed provide critical support for quantifying the expansion behavior of CaO and MgO-based compound expansive agents in the vault of CFST arch bridges.

Article history: Received Mar 21, 2024; Accepted Jul 17, 2024

KEYWORDS CFST, autogenous shrinkage, restriction, expansion agent, principle of creep superposition

1 Introduction

Concrete-filled steel tubes (CFST) have garnered favor within the engineering community due to their distinctive load-bearing capabilities [1], particularly in the domain of arch bridges [2–4]. In recent years, China has witnessed the construction of CFST arch bridges with spans exceeding 300 m, as depicted in Table 1. Capitalizing on the superb compressive strength and streamlined construction attributes of CFST, the development of 300 m span CFST arch bridges commenced as early as 2000. By 2005, a significant milestone was reached with a span of 460 m, and this achievement was further extended to 530 m within the following eight years. As arch bridge spans continue to expand, so too does the complexity of their construction, placing heightened demands on engineering expertise. Over the subsequent seven years, during the construction of the Pingnan Third Bridge, the span of CFST arch bridges escalated to 575 m. Presently, with the ongoing construction of the Tian'e Longtan Bridge, the anticipated span of CFST arch bridges is poised to breach the 600 m threshold [4]. The rugged terrain of western China necessitates CFST arch bridges with elevated rigidity and outstanding durability. However, catering to the demands of these challenging environments remains a formidable task, especially for 600-m-class span bridges. Consequently, the advancement of CFST arch bridge technology necessitates a commensurate evolution in academic research [5].

The development of CFST arch bridge spans is challenged by a significant hazard known as CFST debonding, which severely compromises the bearing capacity of the structure and poses potential safety risks [6–10]. This debonding issue tends to accumulate in the arch crown due to the horizontal orientation of the arch crown and the inability to vibrate the core concrete of closed CFST during construction [11]. Additionally, during the plastic stage, air bubbles trapped within the core concrete rise and accumulate at the top, exacerbating the debonding of the arch crown due to both core concrete bleeding and their presence [7]. In the subsequent hardening and service stage of CFST, the

Table 1 List of concrete filled steel tubular arch bridges built in China (span ⩾ 300 m)

Number	Bridge name	Type	Built-up year	Span (m)	Cross-section	Construction method
1	Third Pingnan Bridge	half through	2020	575	four-tube truss	cable swing, cable-stayed fastening
2	Yangtze River Bridge	half through	2013	530	four-tube truss	cable swing, cable-stayed fastening
3	Hejiang Yangtze River Highway Bridge	flying swallow	2021	507	four-tube truss	cable swing, cable-stayed fastening
4	Wushan Yangtze River Bridge	half through	2005	460	four-tube truss	cable swing, cable-stayed fastening
5	Guizhou Daxiaojing Super Bridge	deck arch	2019	450	four-tube truss	cable swing, cable-stayed fastening
6	Tibet Yarlung Zangbo River Bridge	half through	2020	430	four-tube truss	cable swing, cable-stayed fastening
7	Hurongxi Expressway Zhijing River Bridge	deck arch	2009	430	four-tube truss	cable swing, cable-stayed fastening
8	Liangshuigou Bridge	deck arch	2009	430	four-tube truss	cable swing, cable-stayed fastening
9	Xiangtan Liancheng Bridge	cable-stayed-fly-bird-type	2007	388	six-tube truss	cable swing, cable-stayed fastening
10	Zhunshuo Railway Yellow River Bridge	deck arch	2015	380	four-tube truss	cable swing, cable-stayed fastening
11	Yiyang Maocao Street Bridge	fly-bird-type	2005	368	four - tube truss	cable swing, cable-stayed fastening
12	Guizhou Zongxi River Bridge	deck arch	2014	360	four-tube truss	cable swing, cable-stayed fastening
13	Guangzhou Yajisha Bridge	fly-bird-type	2000	360	six-tube truss	cable swing, cable-stayed fastening
14	Hurongxi Expressway Xiao River Bridge	deck arch	2009	338	six-tube truss	cable swing, cable-stayed fastening
15	Matan Red River Bridge	half through	2018	336	four-tube truss	cable swing, cable-stayed fastening
16	Anhui Huangshan Taiping Lake Bridge	half through inner basket handle	2007	336	horizontal dumbbell truss	cable swing, cable-stayed fastening
17	Nanning Yonghe Bridge	half through	2004	335	horizontal dumbbell truss	cable swing, cable-stayed fastening
18	Chun'an Nanpu Bridge	half through	2003	308	four-tube truss	cable swing, cable-stayed fastening
19	Guizhou Xianghuoyan Super Bridge	deck arch	2017	300	heightened six-tube truss	cable swing, cable-stayed fastening

sharp shrinkage of high-strength core concrete [12] and the disparity in Poisson's ratio between the two materials [8] may also contribute to debonding.

To mitigate CFST debonding, scholars have proposed various solutions, including the incorporation of expansion agents [13–22], internal curing materials [16], and fibers [14,16,19,20,23] to facilitate and compensate for shrinkage, respectively. A CFST extrusion test conducted by Lu et al. [14] under varying expansion agent content revealed that self-stress presence led to an average 42.7% increase in bond strength. According to Chang et al.'s study [15], self-stress can enhance bond strength by 1.2 to 3.3 times. Extensive research has also focused on exploring the ultimate bearing capacity of CFST. Shen et al. [16] studied the synergistic effect of internal curing materials and expansion agents to prepare core concrete with high residual expansion and exceptional compressive strength, suitable for CFST applications. Huang et al.'s research [17] demonstrated that incorporating an expansion agent significantly enhanced the axial compressive properties of CFST, leading to yield hardening. Ho et al. [18] showed that adding a 20% expansion agent enhanced the elastic modulus, yield strength, and ultimate strength of CFST. Li et al. [19] investigated the axial compressive properties of calcium sulfoaluminate cement and ordinary Portland cement CFST, finding that the presence of self-stress significantly restrained axial shortening while enhancing bearing capacity by 9.8% to 27.6%. Xu et al. [24] studied the axial compressive deformation of CFST specimens and observed that varying expansion agent content (0%–10%) resulted in self-stress-induced co-deformation of early core concrete under lateral confinement, leading to significant load sharing by the core concrete. These studies have primarily focused on investigating the mechanical characteristics of self-stressed CFST subjected to expansion agents, making the correlation between self-induced stress and the adhesive strength/load-bearing capacity of CFST clearer, and recognizing the advantageous effects of expansion agents on CFST.

However, limited research currently exists on the volume deformation of core concrete in CFST, and the investigation into the expansion behavior of expansion agents within the steel tube is still in its early stages. Li et al. [25] incorporated CaO and MgO compound expansion agents into vertically positioned CFSTs and investigated their radial and axial free and constrained deformations of the steel tube. The findings indicate that despite the reduction in expansion value due to the steel tube constraint, the calcium-magnesium composite expansion agent still offers sufficient expansion capacity to maintain the integrity of CFST. In horizontal sections with a high potential for debonding in CFST arch bridges, the predominant form of debonding is mostly spherical crown, which differs from vertically placed specimens where circumferential debonding occurs more frequently. Therefore, the current research on vertical specimen expansion development is insufficient to serve as a reference for debonding treatment of the arch crown. Investigating the contraction compensation and debonding relief effects of expansion agents in horizontal CFST structures is imperative. The expansion agent can only induce significant overall expansion in the concrete after it has attained sufficient strength and elastic modulus [26,27]. Prior to this, the core concrete has already detached from the steel tube in the upper section due to plastic shrinkage or bleeding. Before it can generate self-stress on the steel tube, the void needs to be filled with core concrete. The current calculation of CFST compensation shrinkage fails to account for this factor, resulting in the expansion agent often meeting laboratory requirements but exhibiting poor performance in actual applications. Furthermore, the utilization of expansion agents to mitigate core concrete shrinkage has been acknowledged in a significant number of CFST arch bridge projects [5,28,29]. During the prolonged construction period of CFST arch bridges, after the completion of concrete pouring in the tube, it is also imperative to install the hanger and bridge slab before opening it to traffic, a process that typically takes approximately six months to one year. The stability of the expansion development of core concrete under long-term constraints and the maintenance of self-stress are crucial considerations in practical projects. While the creep behavior of CFST under axial load has been extensively investigated in numerous studies [30–36], there is currently no available literature on the long-term creep development of self-stress in the core concrete when subjected to steel tube confinement. Quantitatively characterizing the long-term expansion behavior of the expansion agent in CFST arch bridges under the constraint of steel tubes warrants further investigation to determine whether self-stress will gradually subside or remain stable for an extended period.

To address these gaps in research, this paper derives a creep model for the expansion development of core concrete under constrained conditions based on principles of elastic mechanics and linear creep mechanics. Subsequently, it conducts long-term monitoring of 114 d to observe the deformation of full-size CFST core concrete with horizontally placed undoped and doped expansion agents, revealing the chronological development of concrete expansion within the tube and validating the creep model. In this research process, the paper aims to achieve four primary research objectives: 1) explore the debonding gap caused by plastic shrinkage or air entrapment in the plastic stage of core concrete; 2) study the long-term creep behavior of concrete radial expansion constrained by a steel tube and establish a creep model; 3) investigate the expansion behavior and

long-term development of expansion agents in the axial direction in addition to the radial deformation of core concrete; 4) examine the disparity and correlation between the development of the expansion process and the ultimate expansion of the core concrete in both laboratory and steel tube settings. Subsequently, incorporating deformation data from laboratory specimens into the model is proposed to enhance its applicability range.

2 Mechanical mechanism of radial expansion of core concrete

The mechanical mechanism behind the radial expansion of the core concrete in CFST structures is a crucial aspect of this study. Often, due to the influence of early plastic shrinkage, significant debonding occurs inside CFST during pouring, as illustrated in Fig. 1. The expansion development of the core concrete can be classified into two distinct stages: the debonding stage and the subsequent restriction stage, based on the extent to which the steel tube limits its impact on the concrete.

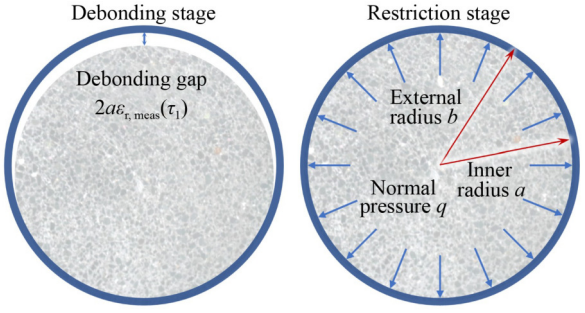

Fig. 1 Calculation model of core concrete expansion in CFST.

During the debonding stage, the primary role of the expansion agent is to compensate for debonding gaps. In this phase, the steel tube has minimal influence on deformation development. However, in the latter stage, the core concrete gradually fills the debonding gap, and the expansion deformation is subject to effective constraints imposed by the steel tube. This encompasses both instantaneous (elastic) and long-term restrictions (creep).

The entire expansion process of the core concrete revolves around four critical variables. These variables encompass the total deformation $\varepsilon_{r,tot}(t)$ of the stress-free concrete, the radial deformation $\varepsilon_{r,meas}(t)$ measured by the sensor within the core concrete, and two values employed in mechanical calculations: $\varepsilon_{r,exp}(t)$, representing the expansion effect of core concrete on the steel tube under restricted conditions, and $\varepsilon_{rc}(t)$, denoting the radial strain of core concrete at the restriction stage (where subscript r indicates the radial direction). The ideal development curve for these four variables is depicted in Fig. 2.

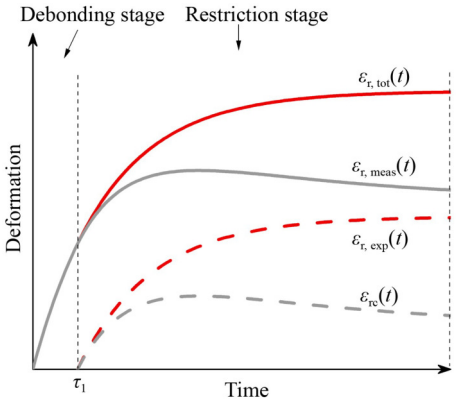

Fig. 2 Four typical parameters in the two-stage expansion process of core concrete.

During the debonding stage, owing to the minimal degree of restriction, there is little difference between $\varepsilon_{r,tot}(t)$ and $\varepsilon_{r,meas}(t)$, while both $\varepsilon_{r,exp}(t)$ and $\varepsilon_{rc}(t)$ are essentially zero. However, it's important to note that limitations imposed by steel tubes cannot be disregarded during the restriction stages, resulting in a gradual decrease in $\varepsilon_{r,meas}(t)$ in comparison to $\varepsilon_{r,tot}(t)$. Additionally, $\varepsilon_{rc}(t)$ is also smaller than $\varepsilon_{r,exp}(t)$.

To quantitatively describe the deformation process of core concrete, a mathematical model has been established to simulate the entire expansion process. This model is based on the following assumptions.

1) The restriction effect of the steel tube on the deformation of core concrete is disregarded during the debonding stage, implying that $\varepsilon_{r,meas}(t) = \varepsilon_{r,tot}(t)$.

2) Since the restriction effect of the steel tube on the core concrete during the debonding stage is not considered, both $\varepsilon_{r,exp}(t)$ and $\varepsilon_{rc}(t)$ are assumed to be zero during this stage. In other words, the steel tube is not subjected to circumferential expansion force during the debonding stage.

3) The time point that marks the division between the two stages is denoted as τ_1. At this point, the debonding gap measures $2a\varepsilon_{r,meas}(\tau_1)$. Furthermore, the relationship between the core concrete strain $\varepsilon_{rc}(t)$ and the sensor-measured concrete deformation $\varepsilon_{r,meas}(t)$ in both stages satisfies Eq. (1). Meanwhile, the relationship between the expansion $\varepsilon_{r,exp}(t)$ generated by core concrete on the steel tube and the total deformation $\varepsilon_{r,tot}(t)$ under freedom conditions satisfies Eq. (2).

$$\begin{cases} \varepsilon_{rc}(t) = 0, & 0 \leqslant t < \tau_1, \\ \varepsilon_{rc}(t) = \varepsilon_{r,meas}(t) - \varepsilon_{r,meas}(\tau_1), & t \geqslant \tau_1, \end{cases} \tag{1}$$

$$\begin{cases} \varepsilon_{r,exp}(t) = 0, & 0 \leqslant t < \tau_1, \\ \varepsilon_{r,exp}(t) = \varepsilon_{r,tot}(t) - \varepsilon_{r,tot}(\tau_1), & t \geqslant \tau_1. \end{cases} \tag{2}$$

4) It is assumed that the total expansion displacement of the core concrete always surpasses the debonding gap, leading to the generation of expansion force on the steel

tube. In simpler terms, there exists a value t such that $t \geqslant \tau_1$.

2.1 Radial expansion stress of concrete-filled steel tube based on elastic mechanics

Once the core concrete makes full contact with the steel tube and undergoes stress, it enters the restriction stage. During this stage, the stress in both the core concrete and steel tube can be calculated using principles of mechanics. We assume an expansion deformation $\varepsilon_{r,exp}$ within the core concrete and a close connection between the inner wall of the steel tube and the concrete:

$$\varepsilon_{r,exp} a + (u_{rc}^{e})_{r=a} = (u_{rs}^{e})_{r=a}, \tag{3}$$

where the expansion deformation generated by the core concrete is denoted as $\varepsilon_{r,exp}$, and a represents the inner radius of the steel tube, which corresponds to the radius of the core concrete. The displacement of the concrete is represented as u_{rc}^{e}, while u_{rs}^{e} represents the displacement of the steel tube. In polar coordinates, Eq. (4) can be used to express both displacements.

$$\begin{cases} u_{rc}^{e} = \dfrac{1+\mu_c}{E_c}\left[2(1-2\mu_c)C_c r - \dfrac{A_c}{r}\right] + I_c \cos\theta + K_c \sin\theta, \\ u_{rs}^{e} = \dfrac{1+\mu_s}{E_s}\left[2(1-2\mu_s)C_s r - \dfrac{A_s}{r}\right] + I_s \cos\theta + K_s \sin\theta, \end{cases} \tag{4}$$

where the Poisson ratios of concrete and the steel tube are denoted as μ_c and μ_s, respectively. The variables r and θ represent the radius and angle in polar coordinates. E_c and E_s refer to the elastic moduli of concrete and the steel tube, respectively. A_c, A_s, C_c, C_s, I_c, I_s, K_c, and K_s are constants.

The steel tube is treated as a thick-walled cylinder with an inner radius 'a' and an outer radius 'b', while the concrete is considered a thick-walled cylinder with an outer radius 'a' and an inner radius of zero. Due to the central symmetric nature of CFST, I_c, I_s, K_c, and K_s are all equal to zero. Assuming that q represents the pressure between the steel tube and core concrete as depicted in Fig. 1, the parameters A_c, A_s, C_c, and C_s in Eq. (4) can be determined as follows:

$$\begin{cases} A_c = 0, \\ 2C_c = -q, \end{cases} \tag{5}$$

$$\begin{cases} A_s = -\dfrac{a^2 b^2 q}{b^2 - a^2}, \\ 2C_s = \dfrac{a^2 q}{b^2 - a^2}. \end{cases} \tag{6}$$

The combination of Eq. (3) to Eq. (6) yields:

$$\varepsilon_{r,exp} = q\left[\frac{(1+\mu_c)(1-2\mu_c)}{E_c} + \frac{(1+\mu_s)(1-2\mu_s)a^2 + (1+\mu_s)b^2}{E_s(b^2-a^2)}\right]. \tag{7}$$

From this, the total radial strain $\varepsilon_{rc}^{e} + \varepsilon_{r,exp}$ of core concrete can be obtained:

$$\varepsilon_{rc}^{e} + \varepsilon_{r,exp} = \frac{1-\mu_c^2}{E_c}\left(\sigma_{rc}^{e} - \frac{\mu_c}{1-\mu_c}\sigma_{\theta c}^{e}\right) + \varepsilon_{r,exp} = \left(1 - \frac{(1+\mu_c)(1-2\mu_c)}{E_c\left[\dfrac{(1+\mu_c)(1-2\mu_c)}{E_c} + \dfrac{(1+\mu_s)(1-2\mu_s)a^2 + (1+\mu_s)b^2}{E_s(b^2-a^2)}\right]}\right)\varepsilon_{r,exp}. \tag{8}$$

The σ_{rc}^{e} denoted as radial stress of core concrete, and $\sigma_{\theta c}^{e}$ denoted as the circumferential stress of core concrete. By determining the parameter k_r that satisfies Eq. (9), the expression for the radial strain of concrete can be obtained using Eq. (10).

$$k_r = 1 - \frac{(1+\mu_c)(1-2\mu_c)}{E_c\left[\dfrac{(1+\mu_c)(1-2\mu_c)}{E_c} + \dfrac{(1+\mu_s)(1-2\mu_s)a^2 + (1+\mu_s)b^2}{E_s(b^2-a^2)}\right]}, \tag{9}$$

$$\varepsilon_{rc}^{e} + \varepsilon_{r,exp} = k_r \varepsilon_{r,exp}. \tag{10}$$

When $r = b$, the circumferential strain $\varepsilon_{\theta s}^{e}$ of the steel tube is obtained:

$$\varepsilon_{\theta s}^{e} = \frac{1-\mu_s^2}{E_s}\sigma_{\theta s}^{e} = \frac{2(1-\mu_s^2)}{E_s\left(\dfrac{b^2}{a^2}-1\right)\left[\dfrac{(1+\mu_c)(1-2\mu_c)}{E_c} + \dfrac{(1+\mu_s)(1-2\mu_s)a^2 + (1+\mu_s)b^2}{E_s(b^2-a^2)}\right]}\varepsilon_{r,exp}, \tag{11}$$

where $\sigma_{\theta s}^{e}$ is the circumferential stress of the steel tube. Given the parameter k_s so that it satisfies Eq. (12), the

circumferential strain of the steel tube can be expressed as Eq. (13).

$$k_s = \frac{2(1-\mu_s^2)}{E_s\left(\frac{b^2}{a^2}-1\right)\left[\frac{(1+\mu_c)(1-2\mu_c)}{E_c}+\frac{(1+\mu_s)(1-2\mu_s)a^2+(1+\mu_s)b^2}{E_s(b^2-a^2)}\right]}, \tag{12}$$

$$\varepsilon_{\theta s}^{e} = k_s \varepsilon_{r,exp}. \tag{13}$$

Thus, by considering the specific radial expansion $\varepsilon_{r,exp}$, we can determine the respective strains of both concrete and steel tube in their elastic state. In case $\varepsilon_{r,exp}$ varies over time (i.e., $\varepsilon_{r,exp}(t)$), the previously obtained strains and stresses will also undergo temporal changes.

2.2 Radial expansion stress of concrete-filled steel tube based on linear creep mechanics

Over an extended service period, the confined stress within the steel tube induces creep in the core concrete, resulting in the gradual attenuation of both radial expansion deformation and stress. Due to the imperfections in creep mechanisms, various long-term prediction models have been developed, including exponential, logarithmic, power functions, hyperbolic functions, and combinations thereof [37]. Considering the advantageous mathematical properties of the exponential function in stress calculation, this paper adopts the creep form based on the exponential function. Therefore, for the restriction stage, the core concrete's creep function is defined as follows [38–40]:

$$C(t,\tau) = \left(C_0 + \frac{A}{\tau}\right)\left(1 - e^{-\gamma(t-\tau)}\right). \tag{14}$$

In this equation, $C_0 + A/\tau$ represents the continuous aging of the core concrete with time, and $1 - \exp(-\gamma(t - \tau))$ represents the continuous decay of creep with time under load. Here, τ represents the initial time of creep, and A, C_0, γ are constants. t represents the age of the core concrete. Since the core concrete is exposed to sealed conditions, only its basic creep is considered. Additionally, given that the restriction force of the steel tube is significantly less than 0.4 times the compressive strength of the core concrete, it is reasonable to assume that the stress and creep exhibit a linear relationship. Therefore, Boltzmann's superposition principle [41–43] is applicable to the creep deformation under various stress histories. The radial deformation of the core concrete, $\varepsilon_{rc}^{c}(t)$ considering creep, can be calculated using Eq. (15).

$$\varepsilon_{rc}^{c}(t) = \frac{1-\mu_c^2}{E_c(t)}\left[\sigma_{rc}(t) - \frac{\mu_c}{1-\mu_c}\sigma_{\theta c}(t)\right] + (1-\mu_c^2) \cdot \int_{\tau_1}^{t}\left[\sigma_{rc}(\tau) - \frac{\mu_c}{1-\mu_c}\sigma_{\theta c}(\tau)\right]\frac{\partial}{\partial\tau}\left(\frac{1}{E_{c0}} + C(t,\tau)\right)d\tau. \tag{15}$$

The first part of left-hand side in the aforementioned equation represents the elastic term, while the second part represents the creep term. As $u_{rc}(t) = r\varepsilon_{rc}^{c}(t)$, Eq. (3), when taking creep into account, should be expressed as follows:

$$\begin{aligned}&\varepsilon_{r,exp} + \frac{1+\mu_c}{E_c(t)}[-(1-2\mu_c)q(t)] \\ &+ (1-\mu_c^2)\int_{\tau_1}^{t}[-(1-2\mu_c)q(\tau)]\frac{\partial}{\partial\tau}C(t,\tau)d\tau \\ &= \frac{1+\mu_s}{E_s}\left[(1-2\mu_s)\frac{a^2q(t)}{b^2-a^2} + \frac{b^2q(t)}{b^2-a^2}\right].\end{aligned} \tag{16}$$

Equation (17) can be obtained by a simple transposition operation from Eq. (16).

$$\frac{\varepsilon_{r,exp}}{\left[\frac{(1+\mu_c)(1-2\mu_c)}{E_c(t)}+\frac{(1+\mu_s)(1-2\mu_s)a^2+(1+\mu_s)b^2}{E_s(b^2-a^2)}\right]} = q(t) - \frac{(1-\mu_c^2)\int_{\tau_1}^{t}[(1-2\mu_c)q(\tau)]\frac{\partial}{\partial\tau}C(t,\tau)d\tau}{\left[\frac{(1+\mu_c)(1-2\mu_c)}{E_c(t)}+\frac{(1+\mu_s)(1-2\mu_s)a^2+(1+\mu_s)b^2}{E_s(b^2-a^2)}\right]}. \tag{17}$$

Let $k_0(t)$ satisfy Eq. (18), and simplify this creep issue to a stress relaxation problem by considering the concrete elastic modulus as a fixed value E_c. Then, Eq. (17) can be converted to Eq. (19), and $k_0(t)$ can also be simplified to k_0.

$$k_0(t) = \frac{(1-2\mu_c)(1-\mu_c^2)}{\left[\frac{(1+\mu_c)(1-2\mu_c)}{E_c(t)}+\frac{(1+\mu_s)(1-2\mu_s)a^2+(1+\mu_s)b^2}{E_s(b^2-a^2)}\right]}, \tag{18}$$

$$q^{e} = q(t) - k_0\int_{\tau_1}^{t} q(\tau)\frac{\partial}{\partial\tau}C(t,\tau)d\tau. \tag{19}$$

Equation (19) represents a prototypical stress relaxation problem, which can be resolved as Eq. (20).

$$q(t) = q^{e}\left[1 - \gamma k_0\left(C_0 + \frac{A}{\tau_1}\right)\tau_1^{\gamma A k_0}e^{\gamma(1+k_0C_0)\tau_1}\int_{\tau_1}^{t}\frac{e^{-\gamma(1+k_0C_0)\tau}}{\tau^{\gamma A k_0}}d\tau\right]. \tag{20}$$

By determining the relaxation coefficient $K(t)$ that satisfies Eq. (21).

$$K(t)=1-\gamma k_0\left(C_0+\frac{A}{\tau_1}\right)\tau_1^{\gamma A k_0}\mathrm{e}^{\gamma(1+k_0C_0)\tau_1}\int_{\tau_1}^{t}\frac{\mathrm{e}^{-\gamma(1+k_0C_0)\tau}}{\tau^{\gamma A k_0}}\mathrm{d}\tau. \tag{21}$$

And the radial deformation of the steel tube $\varepsilon_{rs}(t)$ can be obtained.

$$\varepsilon_{rs}(t)=\frac{1-\mu_s^2}{E_s}\left[\sigma_{rs}(t)-\frac{\mu_s}{1-\mu_s}\sigma_{\theta s}(t)\right]=\varepsilon_{rs}^{e}K(t). \tag{22}$$

The total radial deformation of concrete, $\varepsilon_{rc}(t)$, is the sum of $\varepsilon^{c}{}_{rc}(t)$ and $\varepsilon_{r,exp}$. Directly applying Eq. (20) to solve for the radial deformation of core concrete in Eq. (15) involves complex operations. However, since the total radial deformation of both concrete and steel tube are equal at $r = a$, it becomes possible to express $\varepsilon_{rc}(t)$ in a similar form as Eq. (22), leading to the derivation of $\varepsilon_{rc}(t)$ as Eq. (23).

$$(\varepsilon_{rc}(t))_{r=a}=(\varepsilon_{rc}^{e})_{r=a}K(t)=k_r\varepsilon_{r,exp}K(t). \tag{23}$$

The long-term creep model of core concrete subjected to confinement from steel tubes has been derived using the equations mentioned above.

3 Raw materials and test methods

The Tian'e Longtan Bridge employs a CFST structure with an inner diameter of 900 m as its stiffness skeleton, onto which the encased concrete is subsequently cast. Core concrete pouring for the CFST was successfully completed on August 10th, 2022, and the construction of the encased concrete was finished on April 30th, 2023. The Tian'e Longtan Bridge was opened to traffic on February 1st, 2024. Before the encased concrete reached sufficient strength, the CFST stiffness skeleton bore the construction load of the arch bridge. However, once the CFST arch ribs were enveloped by encased concrete, any internal defects in the CFST became irreparable. Therefore, our team had to ensure the compactness of the CFST during pouring and guarantee the long-term expansion of the core concrete without debonding. To investigate the long-term creep and expansion behavior of the expansion agent in the CFST before the construction of the Tian'e Longtan Bridge, we designed a full-scale CFST test based on the dimensions of the bridge's arch rib. This test primarily involved measuring the long-term deformation of both the core concrete and the steel tube. Additionally, to ensure the validity of the test, a section of CFST was cut after 114 d to assess the uniformity of its core concrete. The entire testing process is illustrated in Fig. 3.

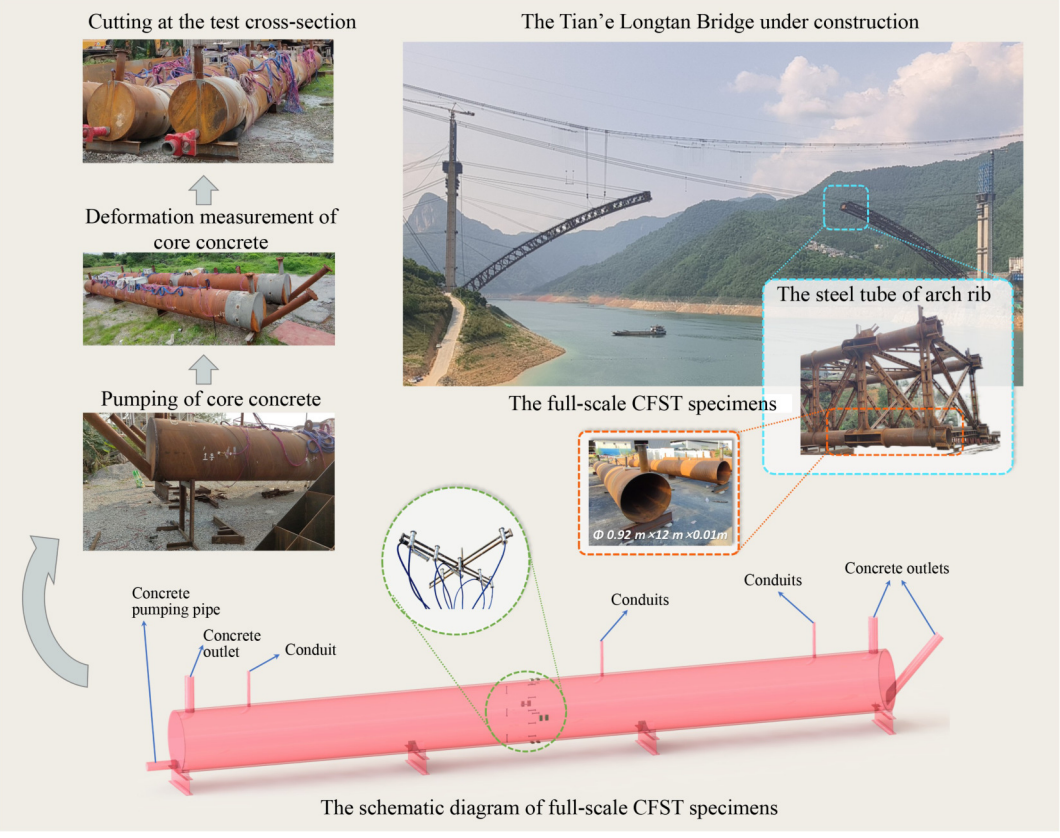

Fig. 3 Schematic diagram of the full-scale experiment.

3.1 Material property

The full-scale experimental design consists of two full-scale CFST specimens, each with a diameter of 0.92 m, a length of 12 m, and a thickness of 0.01 m, as depicted in Fig. 3. The core concrete mix proportion is presented in Table 2. CFST-A serves as the control specimen for investigating the autogenous shrinkage of core concrete, while CFST-B incorporates a 9% expansion agent to examine the shrinkage compensation. The core concrete possesses a strength grade of 70 MPa, and a polycarboxylate superplasticizer is employed to enhance its flowability, ensuring compliance with self-compaction requirements.

The properties of the raw materials used in the full-scale CFST specimens are detailed as follows:

1) P.O 52.5 cement was used;

2) manufactured sand was selected as the fine aggregate, with a fineness modulus of 2.9 and an apparent density of 2.676 g/cm^3;

3) graded diabase crushed stone was used as the coarse aggregate, with an apparent density of 2.959 g/cm^3 and a crush index of 9.8%;

4) the expansion behavior is influenced by factors such as the elastic modulus of the steel tube, based on the aforementioned deduction. Considering economic considerations and given that the elastic modulus of different types of steel is nearly identical, Q235 steel was chosen as the steel tube material for testing purposes [44].

The chemical composition of the cement, silica fume, fly ash, and expansion agent are provided in Table 3. The expansion agent utilized in the experiment is a compound of calcium oxide and lightly burned magnesium oxide. Since the core concrete is enclosed after pouring and experiences high internal temperature rise during its early stages, an expansion agent with a large water demand and high-temperature instability, such as calcium aluminate sulfate [27,45,46], was not chosen. Previous research also supports this approach [25].

3.2 Test methods

3.2.1 Deformation measurement of core concrete

In this study, vibrating-wire strain gauges were employed to capture the spatial distribution of core concrete deformation. These strain gauges had a cylindrical shape, measuring 100 mm in length and 25 mm in diameter. A total of 10 strain gauges were strategically placed in the middle cross-section of the CFST for measurement purposes. Among these, seven strain gauges were arranged in the axial direction and labeled as S1 to S7. The remaining three strain gauges were positioned in the radial direction and designated as S8 to S10. The arrangement of these sensors is depicted in Fig. 4.

The data directly measured by the vibrating-wire strain gauges are the resonant frequency f, and the obtained resonant frequency f can be converted into the deformation results by Eq. (24).

$$\Delta\varepsilon = k_{\mathrm{v}}\Delta f^2 + (a_1 - a_2)\Delta T, \tag{24}$$

where $\Delta\varepsilon$ denotes the calculated deformation change ($\times 10^{-6}$); k_{v} represents a constant, calibrated by the manufacturer; Δf is the change in resonant frequency; a_1 denotes the temperature correction coefficient, which is (13.5×10^{-6}) °C^{-1} according to the calibration from manufacturer; a_2 represents the thermal expansion coefficient of concrete, which is generally (1×10^{-6}) °C^{-1}, ΔT is the change in temperature of the measured points (°C).

3.2.2 Circumferential deformation measurements of steel tube

To measure the circumferential deformation of the CFST-B specimen's steel surface, resistance strain gauges were affixed at four annular positions, as illustrated in Fig. 4. After installing the strain gauges, a protective layer of silica gel was applied to minimize potential damage. These four strain gauges were complemented with

Table 2 Mix proportion of the core concrete

Serial number	Water-binder ratio	Cement (kg/m^3)	Silica fume (kg/m^3)	Fly ash (kg/m^3)	Expansion agent (kg/m^3)	Sand (kg/m^3)	Coarse aggregate (kg/m^3)	Water (kg/m^3)	Polycarboxylate superplasticier (kg/m^3)
CFST-A	0.27	505	24	120	0	736	1017	157	11.21
CFST-B	0.27	446	24	120	59	736	1017	157	11.21

Table 3 Chemical composition of the raw materials (%)

Material	CaO	SiO_2	Al_2O_3	Fe_2O_3	MgO	SO_3	TiO_2	BaO	Na_2O	K_2O	LOI
Cement	64.47	19.95	4.62	3.12	2.17	2.55	0.45	–	0.12	0.45	2.0
Fly ash	6.60	48.20	21.11	9.69	4.74	0.46	1.93	0.11	1.84	1.76	2.4
Silica fume	–	95.02	–	–	–	–	–	–	–	–	1.08
Expansion agent	37.2	2.92	3.15	0.48	43.20	9.34	–	2.86	0.12	0.21	0.2

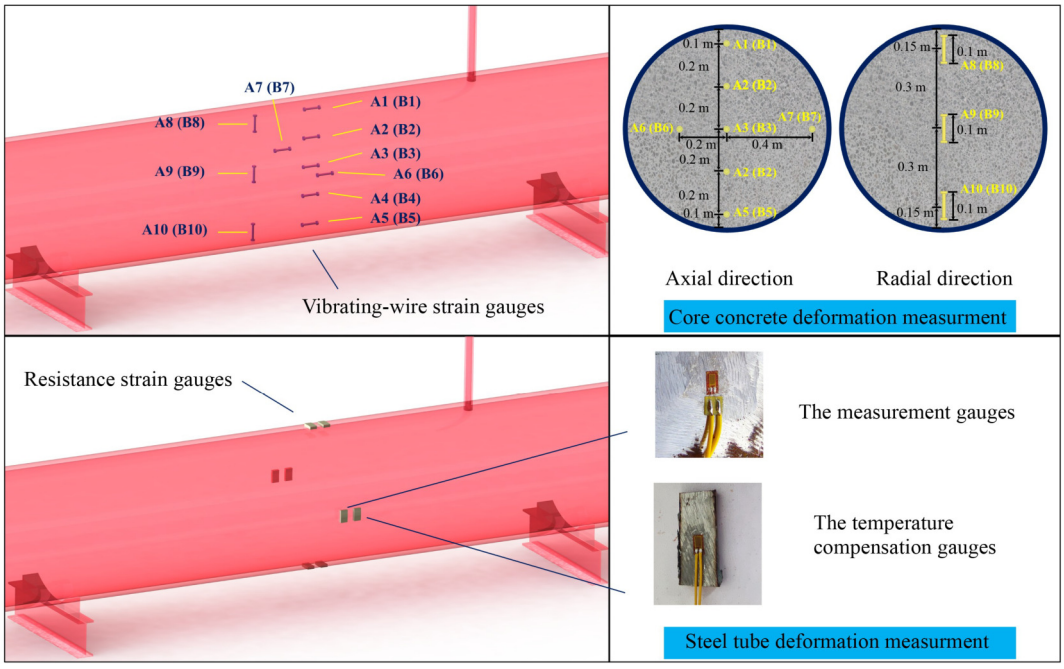

Fig. 4 Deformation measurement arrangements of core concrete and steel tube.

temperature compensation strain gauges, strategically positioned around each gauge. This accounted for the early heat release during concrete hydration and subsequent fluctuations in ambient temperature that could affect the accuracy of deformation measurements. The temperature-compensated strain gauges were mounted on the surface of small steel sheets (1 mm × 10 mm × 20 mm), composed of the same material as the steel tubes. The steel sheet was placed adjacent to its corresponding strain gauge and fully encapsulated with silica gel so that only temperature would affect it. The final deformation results of the steel tube were obtained by subtracting the measurement data of the strain gauge from its respective temperature compensation.

3.2.3 Deformation measurements of laboratory concrete

In addition to the full-size CFST specimen, two groups of prism specimens measuring 515 mm × 100 mm × 100 mm were prepared in the laboratory at a temperature of (20 ± 1) °C to quantify autogenous shrinkage and expansion deformation. Each group consisted of three specimens, and the average test results were recorded. To minimize constraints on the concrete specimens from the mold, oil was applied inside the test mold, and two layers of plastic film were used. Immediately after pouring the concrete, a target was inserted and then covered with plastic film to maintain a sealed condition, as illustrated in Fig. 5. The laser testing system was activated 6 h after the initial setting time of the concrete, and the instrument automatically recorded data every 30 min. After 24 h of pouring, the recording was temporarily halted, and six specimens were demolded to eliminate any influence of

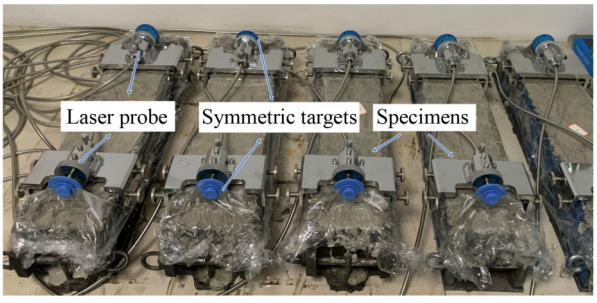

Fig. 5 Deformation measurements of concrete in laboratory.

mold constraints on specimen deformation. Subsequently, data collection resumed for continuous observation.

3.2.4 Mechanical properties and working performance of core concrete

Cube specimens with dimensions of 150 mm × 150 mm × 150 mm and prismatic specimens measuring 100 mm × 100 mm × 300 mm were used to determine the compressive strength and elastic modulus of the concrete, respectively. The measured results are presented in Table 4.

The uniformity of the concrete within the tubes was confirmed by cutting CFST-A and CFST-B specimens at the measured cross-sections after 6 months of pouring. The obtained cross-sections are illustrated in Fig. 6. The cutting position of CFST-A precisely matches the sensor layout location, revealing both the half-cut vibrating-wire strain gauges and a portion of the support. The aggregate ratio was quantitatively analyzed using picture recognition technology in Fig. 7, with 'h' representing the

Table 4 Mechanical properties of core concrete

Number	Compressive strength (MPa)			Elasticity modulus (GPa)		
	3 d	7 d	28 d	3 d	7 d	28 d
CFST-A	54.7	74.2	81.5	29.8	40.1	44.9
CFST-B	56.1	72.6	79.5	28.3	37.5	45.2

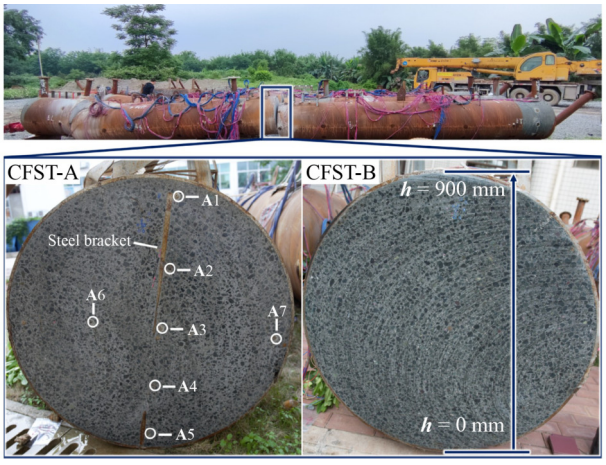

Fig. 6 The cross sections of the full-scale CFST specimens.

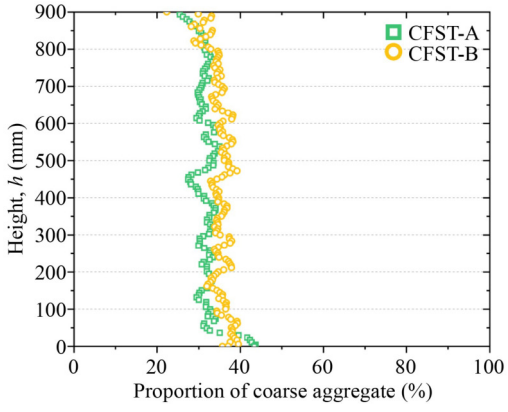

Fig. 7 The distribution of coarse aggregate in the cross sections.

section height ranging from 0 to 900 mm. The aggregate ratio within the cross-section typically falls within the range of 30% to 40%, corresponding to the specified volume fraction in the mix proportion. Overall, both the material selection process and pumping process during testing have proven to be reliable, ensuring a uniform distribution of cement paste and aggregate. Building upon this foundation, the analysis of spatial shrinkage and expansion in the core concrete also demonstrates its effectiveness.

4 Results and discussion

4.1 Radial deformation of core concrete

4.1.1 Radial deformation results and creep model of core concrete

The test results of radial autogenous shrinkage and expansion deformation of core concrete are presented in Fig. 8. It is evident that the autogenous shrinkage and expansion deformation of CFST core concrete exhibit contrasting trends. In the case of CFST-A, the autogenous shrinkage of the lowermost part of the core concrete is intensified by gravity, while the uppermost part undergoes free contraction resulting in minimal shrinkage. Conversely, for the expansion of CFST-B, the effect of gravity results in significantly smaller radial expansion in the lower part of the core concrete compared to the upper and middle parts. This indicates that gravity exerts a restraining effect on concrete expansion.

Referring to previous studies conducted by other researchers [47–49], it can be observed that autogenous shrinkage follows an exponential function form as depicted in Eq. (25).

$$\varepsilon_{\mathrm{G}}(t) = \varepsilon_{\mathrm{G}}\left(1 - \mathrm{e}^{-ct}\right), \tag{25}$$

where $\varepsilon_{\mathrm{G}}(t)$ denotes the shrinkage value of core concrete

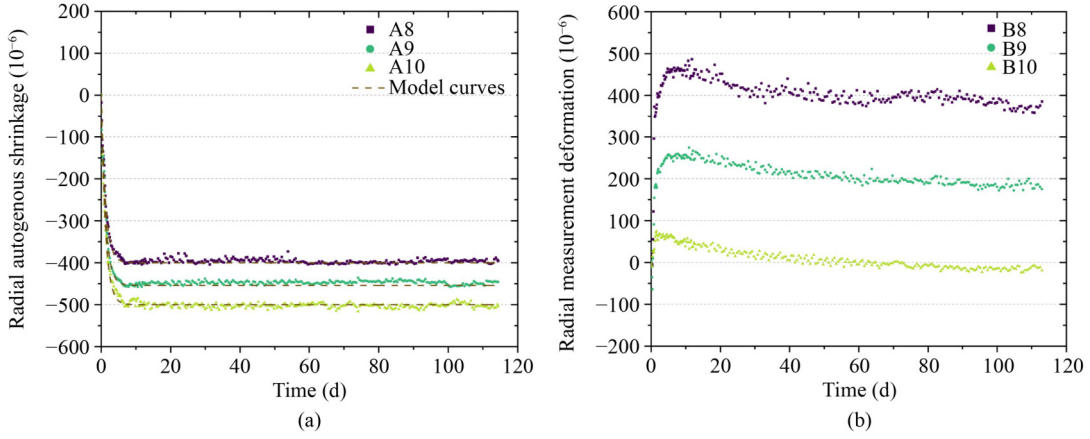

Fig. 8 (a) Radial autogenous shrinkage and its fitting curve of CFST-A and (b) radial measurement deformation of CFST-B.

at time t, ε_G denotes the ultimate shrinkage of core concrete, and c is a constant.

Under unconstrained conditions, the total radial deformation $\varepsilon_{r,tot}(t)$ after adding expansion agent to concrete under unconstrained condition, can be expressed as the summation of autogenous shrinkage $\varepsilon_G(t)$ and expansion $\varepsilon_E(t)$:

$$\varepsilon_{r,tot}(t) = \varepsilon_G(t) + \varepsilon_E(t). \tag{26}$$

Equation (2) indicates that when t is less than τ_1, the radial deformation of core concrete, $\varepsilon_{r,exp}(t) = 0$. However, when $t \geqslant \tau_1$, $\varepsilon_{r,exp}(t) = \varepsilon_{tot}(t) - \varepsilon_{tot}(\tau_1)$. By referring to Eq. (23), we can derive the expression for the long-term creep-induced radial deformation of core concrete as presented in Eq. (27).

$$\begin{cases} \varepsilon_{rc}(t) = 0, & 0 \leqslant t < \tau_1, \\ \varepsilon_{rc}(t) = k_r \varepsilon_{r,exp}(t) K(t) = k_r \left[\varepsilon_{r,tot}(t) - \varepsilon_{r,tot}(\tau_1)\right] K(t), & t \geqslant \tau_1. \end{cases} \tag{27}$$

In fact, Eq. (27) is expressed as $\varepsilon_{rc}(t)$ calculated based on elastic and creep mechanics, whereas the deformation measured by vibrating-wire strain gauges (i.e., the expression of deformation measured in Fig. 8) differs from this expression. In the debonding stage, the measured radial deformation $\varepsilon_{r,meas}(t)$ of the core concrete should be equal to the total radial deformation. While in the restriction stage, the measured deformation was expected to be constrained by the steel tube and exhibited creep behavior, as demonstrated in Eq. (28).

$$\begin{cases} \varepsilon_{r,meas}(t) = \varepsilon_{r,tot}(t), & 0 \leqslant t < \tau_1, \\ \varepsilon_{r,meas}(t) = \varepsilon_{rc}(t) + \varepsilon_{r,tot}(\tau_1) = k_r \left[\varepsilon_{r,tot}(t) - \varepsilon_{r,tot}(\tau_1)\right] K(t) + \varepsilon_{r,tot}(\tau_1), & t \geqslant \tau_1. \end{cases} \tag{28}$$

The expansion development of core concrete can be also considered as an exponential function [50,51]. Therefore, Eq. (28) can be expressed as:

$$\begin{cases} \varepsilon_{r,meas}(t) = \varepsilon_{r,tot}(t) = \varepsilon_{r,G}\left(1 - e^{-c_1 t}\right) + \varepsilon_{r,E}\left(1 - e^{-c_2 t}\right), & 0 \leqslant t < \tau_1, \\ \varepsilon_{r,meas}(t) = \varepsilon_{rc}(t) + \varepsilon_{r,tot}(\tau_1) = k_r \left[\varepsilon_{r,G}\left(1 - e^{-c_1 t}\right) + \varepsilon_{r,E}\left(1 - e^{-c_2 t}\right) - \varepsilon_{r,tot}(\tau_1)\right] K(t) + \varepsilon_{r,tot}(\tau_1), & t \geqslant \tau_1, \end{cases} \tag{29}$$

where $\varepsilon_{r,G}$ and $\varepsilon_{r,E}$ represent the final values of radial shrinkage and expansion of core concrete, respectively, and c_1 and c_2 are constants.

To characterize the deformation of the entire section, the average value of B8–B10 is used to represent the radial deformation of the entire section, denoted as $B_{r,avg}$. Simultaneously, the mean value of the data obtained from the strain gauge after temperature compensation is employed to determine the circumferential strain $\varepsilon_{\theta s}$ of the steel tube, as illustrated in Fig. 9. The circumferential strain of the steel tube goes through three distinct processes: initial flattening, rapid increase, and gradual decrease. Initially, the circumferential strain of the steel tube remains close to 0, but subsequently experiences expansion due to the concrete pressure on its inner surface. Finally, the strain of the steel tube gradually decreases due to the creep of the concrete. The dividing point between the first two processes coincides with the transition from the debonding stage to the restriction stage. In this experiment, the partition time point of the two stages, τ_1, is found to be 0.839 d, with its corresponding $B_{r,avg}(\tau_1)$ at 158.3 × 10^{-6}. This indicates that the initial expansion of concrete fills up the debonding gap of 0.142 mm generated during the plastic stage of concrete. Even for full-size specimens, this debonding gap remains exceedingly small and poses challenges for measurement using conventional detection

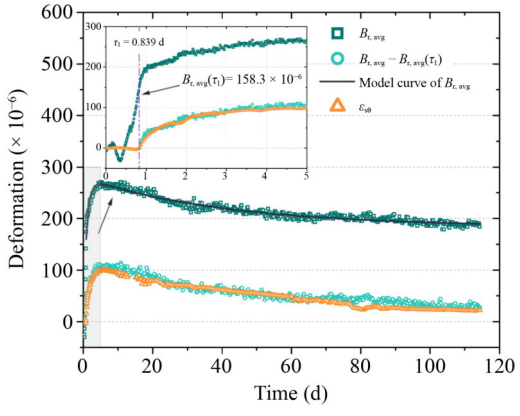

Fig. 9 Average measured radial deformation of core concrete and measured circumferential strain of steel tube.

methods. The findings presented in this paper can serve as valuable references for engineering applications.

By subtracting $B_{r,avg}$ from $B_{r,avg}$ (τ_1), the radial strain ε_{rc} of core concrete in the restriction stage is compared with the circumferential strain $\varepsilon_{\theta s}$ of the steel tube. The development trend of the two is found to be essentially identical. In fact, in the calculation results of the mechanical mechanism part of the paper, it is observed that the circumferential deformation $\varepsilon_{\theta s}$ of the outer surface of the steel tube is proportional to the radial deformation ε_{rc} of the concrete, where $\varepsilon_{\theta s} = 0.948\varepsilon_{r,exp}K(t)$, $\varepsilon_{rc} = 0.901\varepsilon_{r,exp}K(t)$ (the calculation parameters are shown in Table 5, wherein the Poisson ratio and elastic modulus of concrete represent measured values, while those of steel are obtained from the manufacturer). However, the measured circumferential deformation of the steel tube is slightly smaller than the radial deformation of the concrete, which is inconsistent with the calculated results. As the mechanical calculation treats the CFST as a plane strain problem, disregarding axial strain, this may lead to inconsistencies between measured and calculated results. After a measurement period of 114 d, it can be observed that the expansion strain of the steel tube remains at 40×10^{-6}. This indicates that the addition of an expansion agent allows for the long-term maintenance of expansion microstress, ensuring the sustained synergistic effect between the steel tube and concrete.

Based on this, τ_1 is determined to be 0.839 d. Then, Eq. (29) can be employed to fit their respective measured values $\varepsilon_{r,meas}$, and their average values $\varepsilon_{r,avg}$ of B8–B10 in the restriction stage, respectively. First, Eq. (25) is used to fit the core concrete autogenous shrinkage, and parameters $\varepsilon_{r,G}$ and c_1 of each point are determined (refer to Table 6 for details). To ensure convenience in fitting, a uniform value of 0.8 is adopted due to the small difference in c_1 values between each individual shrinkage. Then, by substituting autogenous shrinkage parameters and τ_1 into Eq. (29), the respective parameters $\varepsilon_{r,E}$ and c_2 of the expansion function and the parameters of the relaxation function $K(t)$ can be obtained. The parameters for fitting are listed in Table 6, while the fitting results for each data point and their average result are illustrated in Figs. 10 and 9, respectively. The determination coefficients for each fitting range from 0.78 to 0.96, indicating that the model proposed in this paper exhibits superior capability in accurately capturing the early radial expansion and long-term creep of core concrete constrained by steel tubes.

Table 5 Mechanical calculation parameters

Parameter	Value
μ_c	0.14
μ_s	0.27
E_c (GPa)	37
E_s (GPa)	200
a (m)	0.45
b (m)	0.46

Based on the deformation model presented in this paper, the radial strain of core concrete ε_{cr} (i.e. $B_{r,avg} - B_{r,avg}(\tau_1)$), the circumferential strain of the steel tube $\varepsilon_{s\theta}$, and the interfacial stress q between concrete and the steel tube are calculated. The calculated age t of the concrete ranges from 0.839 to 360 d, equivalent to one year, and the results are illustrated in Fig. 11. The creep predominantly progresses over a period of approximately six months under the specified test conditions outlined in this paper, subsequently reaching a state of stability. In the scenario where the total deformation $\varepsilon_{tot} = \varepsilon_G + \varepsilon_E$ equals 290.1×10^{-6}, 158.3×10^{-6} is utilized to fill the debonding gap resulting from plastic shrinkage, and the subsequent expansion deformation of 131.8×10^{-6} is observed to persist at a level of 26.4×10^{-6} after one-year, indicating a remaining expansion of only 20%.

The maximum interface normal stress q exerted on the steel tube is 0.512 MPa, while the corresponding residual normal stress after one-year amounts to 0.119 MPa, equivalent to a remaining stress of 23%. Therefore, the results indicate that the core concrete of CFST can effectively compensate for shrinkage and induce micro-stresses by incorporating a compound expansion agent consisting of calcium and magnesium oxide. Moreover, even taking into consideration the creep behavior, residual micro-stresses and micro-expansion are retained.

4.1.2 Radial expansion development results and expansion model of core concrete

Based on the fitted parameters $\varepsilon_{r,E}$ and c_2, the expansion development models for each measuring point can be

Table 6 Fitting parameters of core concrete measurement deformation

Deformation	A	E_c	C_0	γ	τ_1	$\varepsilon_{r,G}$ ($\varepsilon_{a,G}$)	c_1	$\varepsilon_{r,E}$ ($\varepsilon_{a,G}$)	c_2	$\varepsilon_{r,tot}(\tau_1)$	R^2
$B_{r,avg}$	1.70×10^{-10}	3.7	0.996	0.00513	0.839	−451.5	0.8	741.6	0.858	158.3	0.95
B8	7.04×10^{-9}	3.7	0.469	0.00944	0.839	−398.5	0.8	885.5	0.914	321.5	0.78
B9	1.03×10^{-16}	3.7	0.400	0.00821	0.839	−454.0	0.8	738.0	0.793	111.3	0.91
B10	0.46914	3.7	6.307×10^{-24}	0.02523	0.839	−502.0	0.8	603.5	0.856	42.0	0.96
$\varepsilon_{ac}(t)$	7.49×10^{-19}	3.7	0.114	0.01961	0.260	−403.3	0.8	859.8	0.721	–	0.97

derived. Since the measured results contained both creep and autogenous shrinkage, the expansion function $\varepsilon_{r,E}(t)$ can be inversely calculated from Eq. (29), as shown in Eq. (30). After inputting the data from points A8–A10 and B8–B10 into Eq. (30) for computation, the radial expansion of the core concrete at each location can be determined. The expansion results and model curves are illustrated in Fig. 12(a), demonstrating a favorable agreement with the exponential model.

$$\begin{cases} \varepsilon_{r,E}(t) = \varepsilon_{r,meas}(t) - \varepsilon_{r,G}(t), & 0 \leqslant t < \tau_1, \\ \varepsilon_{r,E}(t) = \dfrac{\varepsilon_{r,meas}(t) - \varepsilon_{r,tot}(\tau_1)}{k_r K(t)} + \varepsilon_{r,tot}(\tau_1) - \varepsilon_{r,G}(t), & t \geqslant \tau_1. \end{cases} \tag{30}$$

Furthermore, the final expansion value of concrete at different heights exhibits a significant linear relationship with height h, as shown in Fig. 12(b). This indicates the feasibility of utilizing the average value of B8–B10 to represent the mean radial deformation of the section, as mentioned earlier. Based on this, a development model for radial expansion at each height within the core concrete can be established.

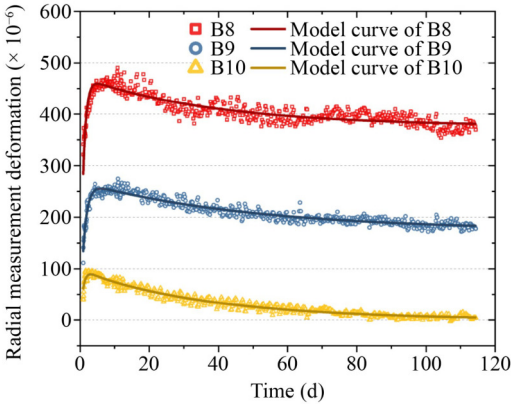

Fig. 10 Radial total deformation distribution and its fitting function at different heights.

$$\begin{cases} \varepsilon_{r,E}(t) = \varepsilon_{r,E}(1 - e^{-c_2 t}), \\ \varepsilon_{r,E} = k_1 \left(\dfrac{h - h_0}{2R} \right) + \varepsilon_{r,E0}, \end{cases} \tag{31}$$

where k_1 is the influence coefficient of gravity, that is, the slope of the straight line in Fig. 12(b), which was measured to be 425.68; $\varepsilon_{r,E0}$ represents the radial expansion of the core concrete at the height of h_0; c_2 is the expansion development coefficient, which is between 0.793 and 0.914 in the test.

4.2 Axial deformation of concrete-filled steel tube core concrete

4.2.1 Measurement results of axial deformation of core concrete and the finite element analysis

The axial deformation of core concrete is presented in Fig. 13, with the initial time selected as 6 h after the completion of pouring. The majority of autogenous

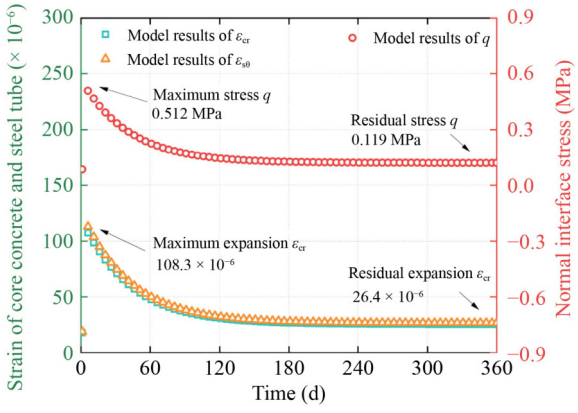

Fig. 11 The axial strain of concrete, the circumferential strain of steel tube and the normal stress of concrete on steel tube within one-year are calculated by proposed creep model.

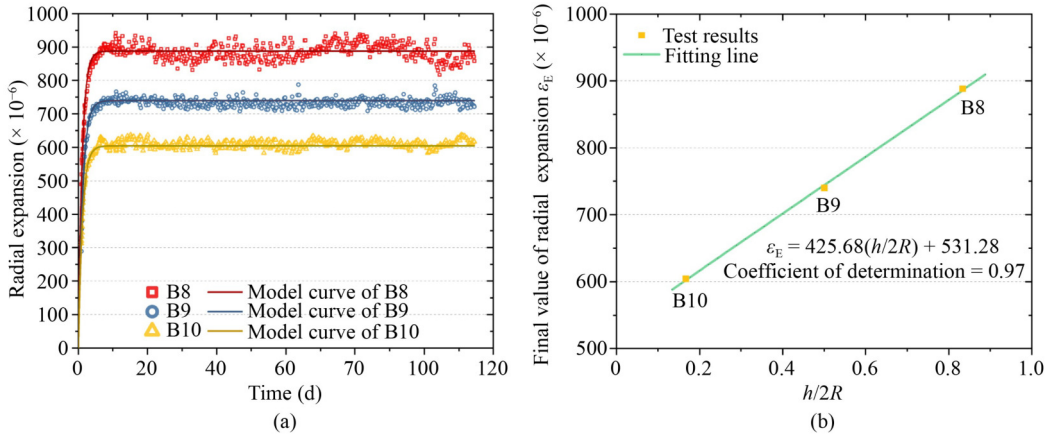

Fig. 12 (a) The distribution of radial total deformation and its fitting function at different heights; (b) the linear correlation of its final expansion value.

shrinkage in concrete without an expansion agent was observed within the initial 6 d, followed by a stabilization of deformation. The axial autogenous shrinkage of core concrete is constrained by the steel tube, exhibiting maximum shrinkage at the midpoint (A3), with decreasing shrinkage closer to the inner surface of the steel tube. Furthermore, no significant creep was observed within the measurement period of 114 d. However, the core concrete deformation of CFST-B exhibits distinct patterns. The deformations measured at points B1–B4 are highly consistent, with only a slight elevation observed at the midpoint (B3) compared to the other three points (B1, B2, and B4). Moreover, the deformation at the bottom point (B5) is approximately 80×10^{-6} lower compared to other regions. To further analyze the stress of both the steel tube and core concrete under autogenous shrinkage and expansion, a finite element model was established, as depicted in Fig. 14(a).

The steel tube has an elastic modulus of 2×10^5 MPa and a Poisson's ratio of 0.27, while the core concrete has an elastic modulus of 3.7×10^4 MPa and a Poisson ratio of 0.14. Due to the relatively low tensile strength of core concrete, it is prone to plastic tensile yielding and even cracking under severe shrinkage. To characterize the softening behavior of core concrete, the Menetrey–Willam model [52] is adopted, in which the yield tensile strength is 3 MPa, the plastic tensile limit strain is 1×10^{-3}, and the residual stress is equal to one-tenth of the tensile strength, i.e., 0.3 MPa. The core concrete was subjected to a shrinkage of 400×10^{-6} (corresponding to the maximum shrinkage measured at midpoint A3) and an expansion of 300×10^{-6} (corresponding to the maximum expansion measured at midpoint B3), respectively, in order to obtain the distribution of axial stress in the section, as depicted in Figs. 14(b) and 14(c). When shrinkage occurs, the concrete experiences axial tensile stress as a result of the steel tube's restraint, leading to certain areas of the concrete exceeding their tensile strength and entering into a plastic softening stage. In contrast, the concrete undergoes axial compressive stress during expansion. Its significantly higher compressive strength compared to tensile strength prevents it from reaching the plastic stage. After selecting a representative section for analysis, it is observed that the axial tensile stress of the core concrete in CFST-A exhibits a phenomenon characterized by higher values at the edges and lower values toward the middle, and the stress gradually decreases from 2.8 to 1.9 MPa. The compressive stress of the core concrete in CFST-B is uniformly distributed throughout the section, measuring approximately −3 MPa (with a negative sign indicating compressive stress). Only a small area near the bottom bearing experiences a slightly higher compressive stress of −5.3 MPa.

In fact, this stress attenuation phenomenon in CFST-A is indeed analogous to the edge interference problem in elastic mechanics, a common occurrence in wall engineering [53]. The constraint effect of the ground

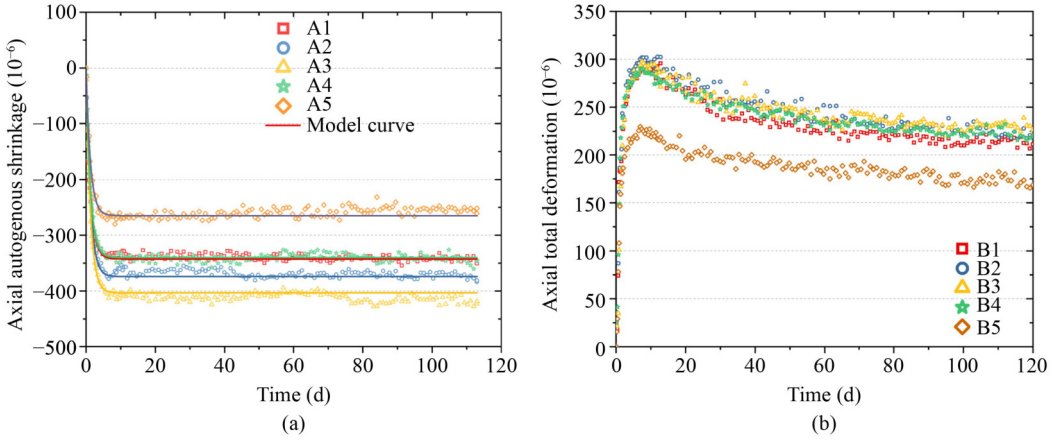

Fig. 13 (a) Axial autogenous shrinkage in CFST-A and (b) axial measured deformation in CFST-B.

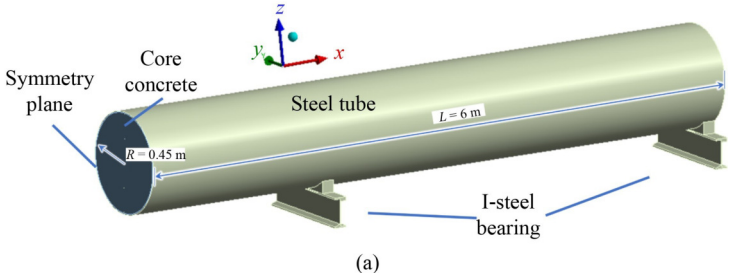

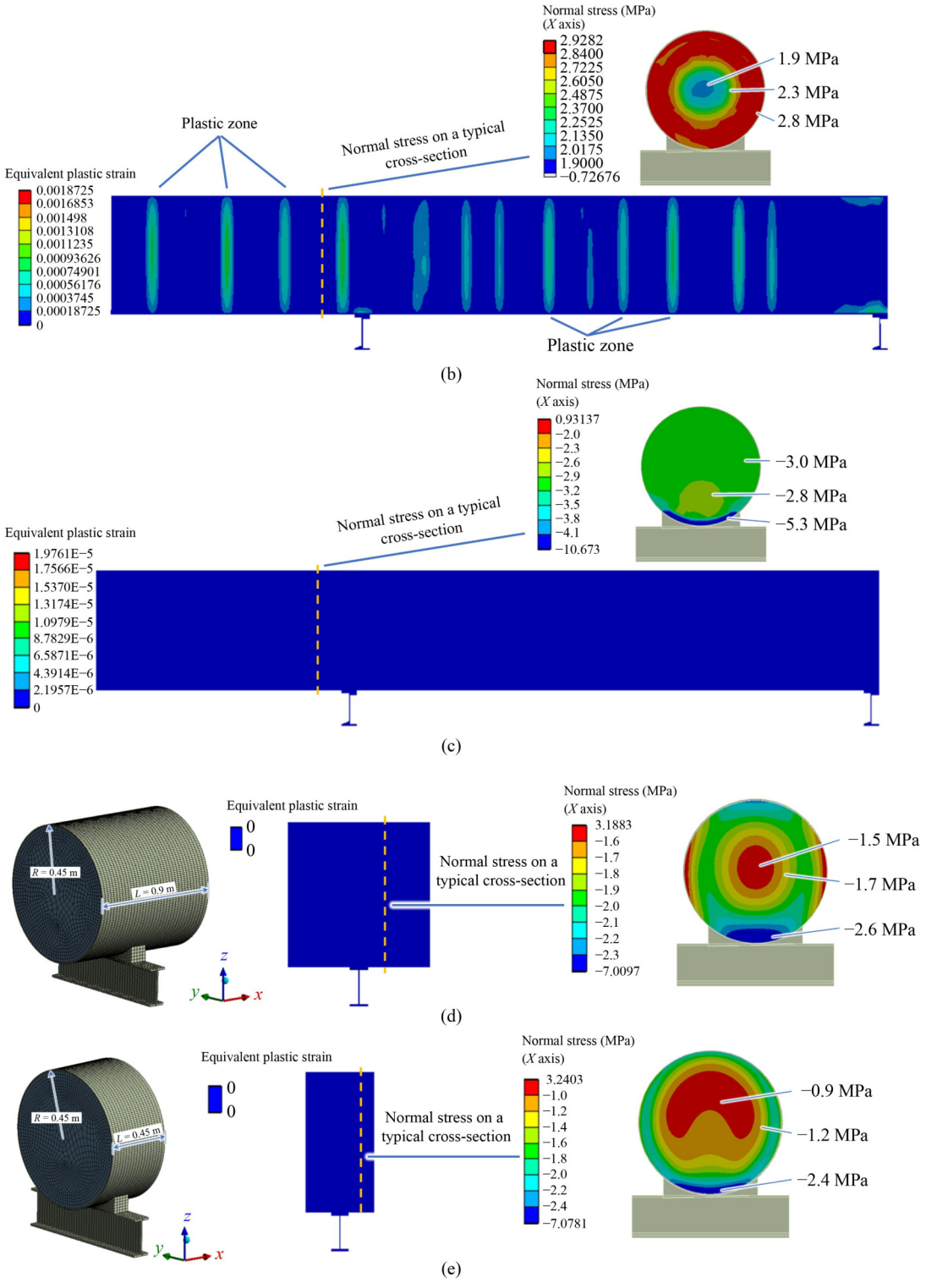

Fig. 14 The equivalent plastic stress and axial stress of core concrete obtained by finite element simulation: (a) the finite element model; (b) 400 × 10^{-6} shrinkage is applied to core concrete; (c) 300 × 10^{-6} expansion is applied to core concrete; (d) 300 × 10^{-6} expansion is applied to CFST when the ratio of radius-to-length (R/L) rises to 0.5; (e) 300 × 10^{-6} expansion is applied to CFST when R/L rises to 1.

foundation on the wall increases as the distance between them decreases, resulting in a greater shrinkage constraint for the wall closer to the foundation and vice versa for those farther away from it. The diminishing impact of this constraint is associated with the H/L ratio, which represents the height-to-length ratio of the wall. A higher H/L value corresponds to a more pronounced decline in constraint effect.

Similarly, CFST can be considered as the concrete core constrained by a steel tube. In CFST, H/L is equivalent to

R/L, which in this test is 0.0375 for the full-size CFST specimen, an extremely small value. As a result, the restraining effect in the test of the steel tube on the core concrete is nearly identical within the same section, resulting in consistent axial stress. For instance, finite element models of CFST specimens with R/L ratios of 0.5 and 1 were established, along with the application of a 300×10^{-6} expansion. The axial stress distribution results are shown in Figs. 14(d) and 14(e). As the ratio of R/L increases, a significant decrease in stress distribution across the cross-section is observed from the periphery toward the center. When R/L = 0.5, the stress decreases from −2.6 to −1.5 MPa, whereas for R/L = 1, the stress reduces from −2.4 to −0.9 MPa, indicating that a higher value of R/L leads to a more pronounced reduction in stress.

Although both specimens CFST-A and CFST-B have an R/L ratio of 0.0375, the core concrete in CFST-A undergoes shrinkage, leading to localized plastic softening and even crack formation. Consequently, the tensile stress load in this region is relieved, causing fragmentation of the core concrete into discrete fragments. As a result, the R/L generally increases to approximately 1, as depicted in Fig. 14(b). In this case, the stress decline effect of the core concrete cannot be ignored, resulting in a reduced confinement from the inner surface of the steel tube to the center of the concrete and a gradual increase in its shrinkage. This is also the essential reason why the deformation distribution of the core concrete was inconsistent when absence or presence of an expansion agent. In other words, the inclusion of an expansion agent altered the stress state of the core concrete, thereby influencing its distribution of deformation. Additionally, this is also the underlying reason why no significant creep was observed in CFST-A. The segmentation of the core concrete into smaller units effectively mitigates the stress exerted by the steel tube, thereby being insufficient to induce noticeable creep behavior. The non-uniformity and non-continuity of the concrete itself may also aggravate the stress attenuation by hindering the effective transfer of shear stress from the steel tube to the concrete center.

4.2.2 Axial stain and expansion model of core concrete

As analyzed above, the R/L ratio of the tested CFST was sufficiently small, indicating that there is minimal change in axial constraint within the same section after the addition of the expansion agent. Therefore, the axial strain model of the core concrete assumes that the strain is uniform across the entire section. Additionally, for simplification purposes, it is assumed that the axial displacement of both the core concrete and steel tube is equal, as follows:

$$\left(\varepsilon_{\mathrm{a,exp}}+\frac{\sigma_{\mathrm{ac}}^{\mathrm{e}}}{E_{\mathrm{c}}}\right)L=\frac{\sigma_{\mathrm{as}}^{\mathrm{e}}}{E_{\mathrm{s}}}L, \tag{32}$$

where $\varepsilon_{\mathrm{a,exp}}$ represents the axial expansion generated by the core concrete, $\sigma_{\mathrm{ac}}^{\mathrm{e}}$ represents the elasticity axial stress of the concrete, $\sigma_{\mathrm{as}}^{\mathrm{e}}$ represents the elasticity axial stress of the steel tube. The equilibrium equation is expressed as:

$$\sigma_{\mathrm{ac}}^{\mathrm{e}}A_{\mathrm{ac}}+\sigma_{\mathrm{as}}^{\mathrm{e}}A_{\mathrm{as}}=0, \tag{33}$$

where A_{ac} and A_{as} represent the cross-section area of the core concrete and steel tube, respectively. By combining Eqs. (32) and (33), the total axial strain of core concrete $\varepsilon_{\mathrm{ac}}^{\mathrm{e}}+\varepsilon_{\mathrm{a,exp}}$ is:

$$\varepsilon_{\mathrm{ac}}^{\mathrm{e}}+\varepsilon_{\mathrm{a,exp}}=\frac{\sigma_{\mathrm{ac}}^{\mathrm{e}}}{E_{\mathrm{c}}}+\varepsilon_{\mathrm{a,exp}}=\left(-\frac{1}{1+\dfrac{a^2E_{\mathrm{c}}}{(b^2-a^2)E_{\mathrm{s}}}}+1\right)\varepsilon_{\mathrm{a,exp}}. \tag{34}$$

Given the parameter k_{a} such that it satisfies Eq. (35), then Eq. (34) can be converted to Eq. (36).

$$k_{\mathrm{a}}=1-\frac{1}{\dfrac{a^2E_{\mathrm{c}}}{(b^2-a^2)E_{\mathrm{s}}}+1}, \tag{35}$$

$$\varepsilon_{\mathrm{ac}}^{\mathrm{e}}=k_{\mathrm{a}}\varepsilon_{\mathrm{a,exp}}. \tag{36}$$

Taking into account the creep, then the problem is similar to the radial creep of core concrete, where Eq. (32) transforms to:

$$\left(\varepsilon_{\mathrm{a,exp}}+\frac{\sigma_{\mathrm{ac}}^{\mathrm{c}}(t)}{E_{\mathrm{c}}(t)}\right)L=\frac{\sigma_{\mathrm{as}}(t)}{E_{\mathrm{s}}}L. \tag{37}$$

The solution is:

$$\sigma_{\mathrm{ac}}^{\mathrm{e}}=\sigma_{\mathrm{ac}}^{\mathrm{c}}(t)+\frac{\displaystyle\int_{\tau_1}^{t}\sigma_{\mathrm{ac}}^{\mathrm{c}}(\tau)\frac{\partial}{\partial\tau}C(t,\tau)\mathrm{d}\tau}{\dfrac{1}{E_{\mathrm{c}}(t)}+\dfrac{a^2}{(b^2-a^2)E_{\mathrm{s}}}}. \tag{38}$$

Let $k'_0(t)$ satisfy Eq. (39), and transform the problem into a stress relaxation scenario, that is, where $E_{\mathrm{c}}(t)$ is considered as a constant E_{c}. Consequently, Eq. (40) can be derived.

$$k'_0(t)=\frac{1}{\dfrac{1}{E_{\mathrm{c}}(t)}+\dfrac{a^2}{(b^2-a^2)E_{\mathrm{s}}}}, \tag{39}$$

$$\sigma_{\mathrm{ac}}^{\mathrm{c}}(t)=\sigma_{\mathrm{ac}}^{\mathrm{e}}\left[1-\gamma k'_0\left(C_0+\frac{A}{\tau_1}\right)\tau_1^{\gamma Ak'_0}\mathrm{e}^{\gamma(1+k'_0C_0)\tau_1}\int_{\tau_1}^{t}\frac{\mathrm{e}^{-\gamma(1+k'_0C_0)\tau}}{\tau^{\gamma Ak'_0}}\mathrm{d}\tau\right]. \tag{40}$$

Similarly, the axial strain of the core concrete can also be expressed as:

$$\varepsilon_{ac}(t) = \varepsilon_{ac}^{e}(t)K'(t) = k_a\left(\varepsilon_{a,G}(t) + \varepsilon_{a,E}(t)\right)K'(t), \quad (41)$$

where $\varepsilon_{ac}(t)$ represents the total axial strain of the core concrete at time t, and $\varepsilon_{a,G}(t)$ and $\varepsilon_{a,E}(t)$ are the free autogenous shrinkage and expansion of the core concrete at time t, respectively. Since the central part of the core concrete has the smallest shrinkage restriction and can best reflect the real free autogenous shrinkage, $\varepsilon_{a,G}(t)$ are taken as the measurement result of A3, and the ultimate shrinkage $\varepsilon_{a,G}$ is 403.3×10^{-6} and c_1 is 0.8. As τ_1 cannot be 0 in the proposed creep model, it is assumed that the creep begins when the concrete finally sets, with τ_1 = 0.26 (time zero is the initial setting time). The value of $\varepsilon_{ac}(t)$ is obtained by averaging the results from points B1 to B4. Equation (41) is employed to fit all the parameters, and the resulting fitting curve is illustrated in Fig. 15. The specific fitting parameters can be found in Table 6.

The expansion development model can be obtained based on the fitting parameters $\varepsilon_{a,E}$ and c_2. Since the measured data contains creep and autogenous shrinkage, the expansion function $\varepsilon_{a,E}(t)$ is extracted from Eq. (41), as shown in Eq. (42). To calculate the average axial expansion development of core concrete, the $\varepsilon_{a,E}(t)$ obtained from collected results is substituted into Eq. (42), as illustrated in Fig. 15. It is indicated that the expansion results are in good agreement with the proposed expansion development model.

$$\varepsilon_{a,E}(t) = \frac{\varepsilon_{ac}(t)}{k_a K(t)} - \varepsilon_{a,G}(t). \quad (42)$$

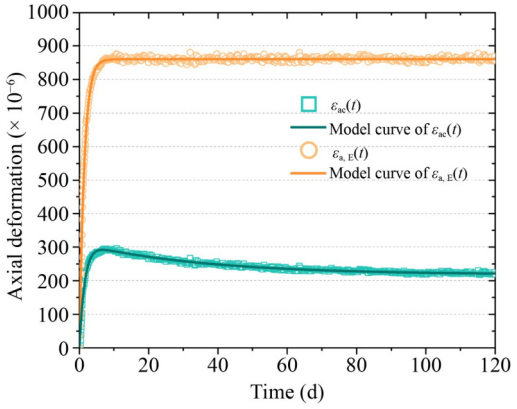

Fig. 15 The measured and model results of the average axial strain of concrete, and the axial expansion calculated from the average axial strain compared model results.

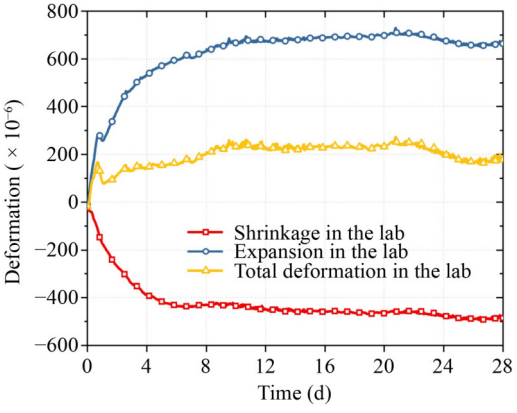

Fig. 16 Autogenous shrinkage and expansion deformation of concrete specimens in the laboratory.

4.3 The incorporation of laboratory specimen deformation into the creep model

4.3.1 Comparison of shrinkage and expansion results between laboratory and core concrete

The laboratory-sealed specimens subjected to constant temperature conditions are depicted in Fig. 16, illustrating the results of shrinkage and expansion. Shrinkage and total deformation are the measured parameters, and the expansion results reflect the difference between them. In the absence of an expansion agent, the concrete displayed substantial shrinkage behavior, which persisted for 28 d. However, the introduction of an expansion agent not only compensated for the shrinkage but also induced some degree of expansion.

Establishing a relationship between the laboratory deformation behavior of core concrete and its real-world performance in CFST is challenging due to practical measurement difficulties. To address this, $\varepsilon_{r,G}(t)$ and $\varepsilon_{a,G}(t)$ are used to represent the shrinkage of core concrete under free-stress conditions. $\varepsilon_{a,G}(t)$ is derived from the minimal steel tube restriction experienced at A3, while $\varepsilon_{r,G}(t)$ is represented by the average shrinkage of A8 to A10. These values are compared to laboratory shrinkage data, as shown in Fig. 17. The laboratory shrinkage is fitted using Eq. (25), resulting in ε_{Glab} of −462.6 and c_2 of 0.43. Notably, the laboratory shrinkage rate is slower, but its ultimate shrinkage at 28 d exceeds that of the core concrete in CFST. This is attributed to the elevated temperature within the CFST core, which accelerates the shrinkage rate while reducing its final magnitude, a phenomenon consistent with prior research [48,54].

Similarly, radial mean expansion $\varepsilon_{r,E}(t)$ (obtained from $B_{r,avg}$) and axial average expansion $\varepsilon_{a,E}(t)$ (obtained from $\varepsilon_{ac}(t)$) are compared with laboratory expansion data in Fig. 17. The laboratory expansion is fitted using Eq. (25), resulting in ε_{Elab} of 682.1 and c_2 of 0.39. The final expansion ε_{Elab} and the development rate c_2 in the laboratory are both lower than those observed in the core concrete. This indicates a slower expansion process and lower final expansion value when subjected to room temperature confinement. This discrepancy can be

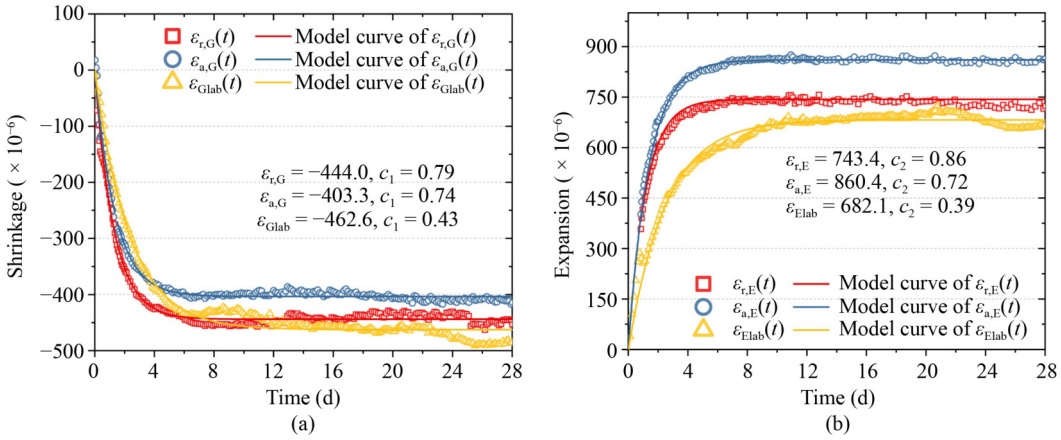

Fig. 17 (a) The shrinkage and (b) expansion and their model curves of concrete in laboratory and in full-scale CFST, respectively.

primarily attributed to the temperature sensitivity of magnesium oxide, which undergoes a more rapid reaction and achieves a higher final expansion when exposed to the elevated curing temperatures within CFST [55,56]. Additionally, gravity effects result in a final radial mean expansion $\varepsilon_{r,E}$ that is 117 × 10^{-6} smaller than the axial mean expansion $\varepsilon_{a,E}$. However, when compared to radial expansion at point S8, which experiences less influence from gravity, it becomes evident that both internal radial and axial expansion magnitudes are similar, measuring approximately 870 × 10^{-6}.

Based on this, the radial and axial average shrinkage (expansion) of the core concrete can be obtained from the shrinkage (expansion) in laboratory. Equations (43) and (44) are obtained by replacing the shrinkage and expansion of core concrete in Eq. (25) with ε_{Glab} and ε_{Elab} measured in the laboratory, respectively.

$$\begin{cases} \varepsilon_{r,G}(t) = \alpha_{rG}\varepsilon_{Glab}\left(1-e^{-\beta_{rG}c_1 t}\right), \\ \varepsilon_{a,G}(t) = \alpha_{aG}\varepsilon_{Glab}\left(1-e^{-\beta_{aG}c_1 t}\right), \end{cases} \tag{43}$$

$$\begin{cases} \varepsilon_{r,E}(t) = \alpha_{rE}\varepsilon_{Elab}\left(1-e^{-\beta_{rE}c_2 t}\right), \\ \varepsilon_{a,E}(t) = \alpha_{aE}\varepsilon_{Elab}\left(1-e^{-\beta_{aE}c_2 t}\right), \end{cases} \tag{44}$$

where α_{rG} (α_{aG}) and β_{rG} (β_{aG}) are temperature coefficients, indicating the impact of temperature on the radial (axial) ultimate shrinkage and its development process. In this test, the values for the radial shrinkage are 1.08 and 2.2, while for the axial shrinkage they are 1.26 and 1.85. Similarly, α_{rE} (α_{aE}) and β_{rE} (β_{aE}) indicate the impact of temperature on ultimate radial (axial) expansion and its development process, respectively. In the radial aspect, 1.08 and 2.2 are taken in this test, and in the axial aspect, 1.26 and 1.85 are taken.

4.3.2 Improvement of the model based on deformation in laboratory

Furthermore, incorporating the laboratory shrinkage and expansion deformation into Eqs. (27) and (41), respectively, yields an improved model for core concrete strain, as demonstrated in Eqs. (45) and (46), correspondingly.

$$\begin{cases} \varepsilon_{rc}(t) = 0, & 0 \leqslant t < \tau_1, \\ \varepsilon_{rc}(t) = k_r\left[\alpha_{rG}\varepsilon_{Glab}\left(1-e^{-\beta_{rG}c_1 t}\right)+\alpha_{rE}\varepsilon_{Elab}\left(1-e^{-\beta_{rE}c_2 t}\right)-\varepsilon_{r,tot}(\tau_1)\right]K(t), & t \geqslant \tau_1, \end{cases} \tag{45}$$

$$\varepsilon_{ac}(t) = k_a\left(\alpha_{aG}\varepsilon_{Glab}\left(1-e^{-\beta_{aG}c_1 t}\right)+\alpha_{aE}\varepsilon_{Elab}\left(1-e^{-\beta_{aE}c_2 t}\right)\right)K'(t). \tag{46}$$

Similarly, by bringing the shrinkage and expansion in the laboratory into Eq. (20), an improved model of the normal stress at steel-concrete interface can be obtained, expressed as Eq. (47).

$$q = \frac{\left[\alpha_{rG}\varepsilon_{Glab}\left(1-e^{-\beta_{rG}c_1 t}\right)+\alpha_{rE}\varepsilon_{Elab}\left(1-e^{-\beta_{rE}c_2 t}\right)-\varepsilon_{r,tot}(\tau_1)\right]K(t)}{\frac{(1+\mu_c)(1-2\mu_c)}{E_c}+\frac{(1+\mu_s)(1-2\mu_s)a^2+(1+\mu_s)b^2}{E_s\left(b^2-a^2\right)}}. \tag{47}$$

The improved model is compared to the test results, which included the radial strain $\varepsilon_{rc}(t)$ (mean value of B8–B10), the axial strain $\varepsilon_{ac}(t)$ (mean value of B1–B4), and the normal stress at steel-concrete interface (obtained

by the circumferential strain $\varepsilon_{\theta s}(t)$ of steel tube). These comparisons are illustrated in Fig. 18. It can be observed that the measured data generally fall within a ±10% error range around the model curve, indicating a strong agreement between the proposed long-term creep model and experimental results.

Furthermore, it's worth noting that a critical parameter in the radial creep model is the expansion $\varepsilon_{r,tot}(\tau_1)$ used to fill the debonding gap, which was determined to be 158.3×10^{-6} in the full-scale test. However, it's important to highlight that quantitatively measuring the early plastic debonding gap within CFST remains a significant challenge, requiring further technical and theoretical research. The results obtained from this experiment can serve as a valuable reference for advancing the research and development of CFST debonding mechanisms. Overall, the full-size test underscores the utility of the proposed creep models, which can accurately predict the long-term radial and axial deformation of core concrete, as well as the normal self-stress at the interface between the steel tube and concrete, based on laboratory deformations of concrete. This capability enables precise quantitative design and construction of CFST structures with controlled micro-expansion or self-stress.

5 Conclusions

In this study, we conducted theoretical and experimental research on the restricted radial and axial expansion behavior of core concrete doped with an expansion agent when CFST is placed horizontally. We proposed a long-term creep model for core concrete and a normal stress model between the steel tube and core concrete based on elastic mechanics and linear creep mechanics, specifically in the debonding stage and the restriction stage. Two full-size CFST specimens were designed and tested to validate our proposed models comprehensively. Our main research findings are as follows.

1) Early plastic shrinkage of the core concrete leads to debonding at the top, necessitating compensation of the debonding gap before the expansion agent applies pressure to the steel tube. This led us to categorize CFST core concrete deformation into the debonding stage and the restriction stage. In our full-scale test, we determined that the transition between these stages occurred at 0.839 d, during which the core concrete experienced an average radial deformation of 158.3×10^{-6} in the debonding stage, filling a debonding gap of 0.142 mm. Notably, quantitatively detecting these small debonding gaps generated during the plasticity period remains challenging using existing detection methods. Therefore, our findings offer valuable insights for further research on CFST debonding and compensation.

2) The radial expansion of the core concrete during the restriction stage results from the combined effects of shrinkage, expansion, and creep. We derived a long-term creep model for the core concrete based on the stress conditions of CFST. Validation through full-scale tests demonstrated that this model accurately represents the long-term deformation behavior of core concrete in the restriction stage. The radial creep of the core concrete was predicted for a period of 360 d, revealing that out of a total deformation value of 290.1×10^{-6}, 158.3×10^{-6} is utilized to fill the debonding gap during the debonding stage. The remaining 131.8×10^{-6} expansion strain maintained a final value of 26.4×10^{-6} after one year, representing a 20% residual, with a corresponding residual normal stress of 0.119 MPa. These findings emphasize that even with concrete creep, expansion agents can maintain their ability to generate micro-stresses on the steel tube to some extent without fully diminishing.

3) We observed variations in the radial deformation of core concrete across its cross-section. The lower part of the core concrete, subjected to gravitational forces, experienced greater radial shrinkage compared to the upper part. Conversely, the lower concrete, influenced by

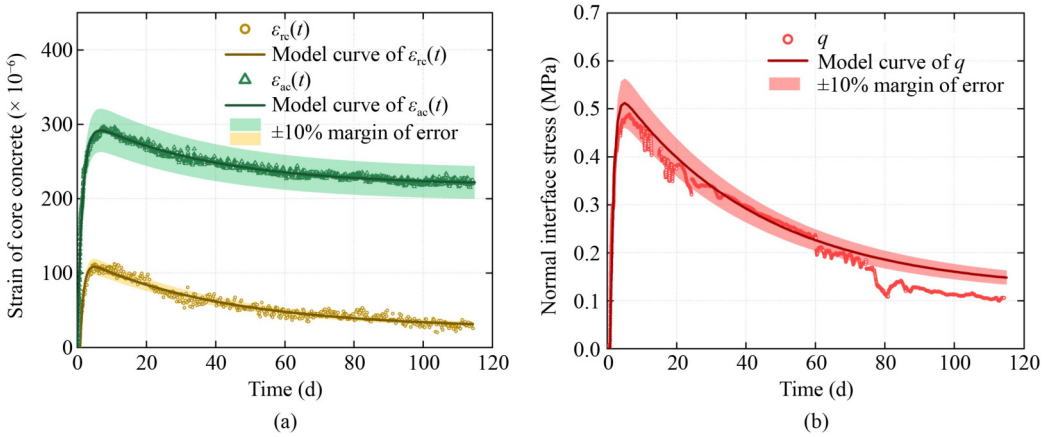

Fig. 18 The agreement between the improved model and the measured data: (a) the strain of core concrete; (b) the normal stress at steel-concrete interface.

gravity, exhibited smaller radial expansion than the upper concrete, with this expansion linearly correlated with height h. Building on these observations, we established time-varying models for the radial expansion of core concrete at different heights.

4) Severe shrinkage can cause the core concrete to fracture into distinct blocks due to tensile softening or damage. This results in an increase in the diameter-to-length ratio (R/L) and a rapid decline in binding force between the steel tube and core concrete along the radial direction. Consequently, greater shrinkage occurs closer to the core concrete's center. The inclusion of an expansion agent can improve the stress state of CFST, preserving its R/L ratio. This maintains relatively constant bond strength between the steel tube and core concrete, resulting in minimal variation in axial expansion within the cross-section. We represented the axial shrinkage and expansion of core concrete using the measured shrinkage at the middle point and the mean expansion measured in full-scale CFST, and we established a long-term creep axial expansion model for core concrete.

5) The core concrete experienced a higher temperature history in its early stages, leading to faster shrinkage and expansion development compared to laboratory specimens. This resulted in ultimately smaller shrinkage and larger expansion of the core concrete, respectively. We incorporated the shrinkage and expansion results obtained from laboratory tests into the radial and axial long-term creep models, as well as the normal stress model at the steel-concrete interface proposed in this paper, enhancing their practical applicability. Our results demonstrated that the measured data generally fell within a ±10% error limit of the improved model, indicating a good agreement.

While our proposed long-term creep model exhibited excellent agreement with measured expansion, further enhancing the theoretical mechanism of the model by considering elastic modulus as a variable remains a challenge. Additionally, reliable methods for verifying whether the debonding gap measures 0.142 mm, as stated, require further advancements in detection technology.

Acknowledgements This research has been financially supported by various institutions, including the National Key Research and Development Program of China (No. 2021YFB2600903), the National Natural Science Foundation of China (Grants Nos. U2006224 and 52368028), the Guangxi Natural Science Foundation, China (No. 2022GXNSFFA035035), the Guangxi Key Research and Development Program (No. GKAB22036007), the Guangxi Science and Technology Major Project (No. GKAA23073017) and the Middle-aged and Young Teachers' Basic Ability Promotion Project of Guangxi (No. 2022KY1159). We express our sincere gratitude for this generous support.

Competing interests The authors declare that they have no competing interests.

References

1. Tang Y, Feng W, Chen Z, Mai J, Zheng J, Yang Y. Behaviour of steel-reinforced recycled aggregate concrete-filled GFRP tubular short columns under eccentric axial compression. Thin-walled Structures, 2024, 199: 111818
2. Chen B, Han L, Qin D, Li W. Life-cycle based structural performance of long-span CFST hybrid arch bridge: A study on arch of Pingnan Third Bridge. Journal of Constructional Steel Research, 2023, 207: 107939
3. Guo C, Lu Z. Effect of circumferential gap on dynamic performance of CFST arch bridges. Journal of Bridge Engineering, 2021, 26(2): 04020121
4. Chen Z, Wu C, Luo X, Xu W, Liang W, Tang Y. Spatio-temporal autogenous shrinkage and cracking behavior of core concrete in full-scale CFST: Insights from the world's largest span arch bridge. Thin-walled Structures, 2024, 200: 111899
5. Zheng J, Wang J. Concrete-filled steel tube arch bridges in China. Engineering, 2018, 4(1): 143–155
6. Chen Z, Jia H, Li S. Bond behavior of recycled aggregate concrete-filled steel tube after elevated temperatures. Construction and Building Materials, 2022, 325: 126683
7. Xue J, Huang J, Fiore A, Briseghella B, Marano G C. Prediction of the mechanical performance of compressed circular CFST columns with circumferential debonding gap. Journal of Constructional Steel Research, 2023, 208: 107988
8. Xue J, Fiore A, Liu Z, Briseghella B, Marano G C. Prediction of ultimate load capacities of CFST columns with debonding by EPR. Thin-walled Structures, 2021, 164: 107912
9. Lu Z, Guo C, Li G. Air void and ring gap effect on CFST arch bridges dynamic performance. Journal of Constructional Steel Research, 2021, 177: 106418
10. Huang Y, Liu A, Fu J, Pi Y. Experimental investigation of the flexural behavior of CFST trusses with interfacial imperfection. Journal of Constructional Steel Research, 2017, 137: 52–65
11. Xue J, Briseghella B, Chen B. Effects of debonding on circular CFST stub columns. Journal of Constructional Steel Research, 2012, 69(1): 64–76
12. Liu H, Chen Z, Liu Y, Chen Y, Du Y, Zhou F. Interfacial debonding detection for CFST structures using an ultrasonic phased array: Application to the Shenzhen SEG building. Mechanical Systems and Signal Processing, 2023, 192: 110214
13. Carballosa P, García Calvo J L, Revuelta D, Sánchez J J, Gutiérrez J P. Influence of cement and expansive additive types in the performance of self-stressing and self-compacting concretes for structural elements. Construction and Building Materials, 2015, 93: 223–229
14. Lu Y, Liu Z, Li S, Li N. Bond behavior of steel fibers reinforced self-stressing and self-compacting concrete filled steel tube columns. Construction and Building Materials, 2018, 158: 894–909
15. Chang X, Huang C, Jiang D, Song Y. Push-out test of pre-stressing concrete filled circular steel tube columns by means of expansive cement. Construction and Building Materials, 2009, 23(1): 491–497

16. Shen P, Lu J, Zheng H, Lu L, Wang F, He Y, Hu S. Expansive ultra-high performance concrete for concrete-filled steel tube applications. Cement and Concrete Composites, 2020, 114: 103813
17. Huang W, Fan Z, Shen P, Lu L, Zhou Z. Experimental and numerical study on the compressive behavior of micro-expansive ultra-high-performance concrete-filled steel tube columns. Construction and Building Materials, 2020, 254: 119150
18. Ho J C M, Ou X L, Li C W, Song W, Wang Q, Lai M H. Uni-axial behaviour of expansive CFST and DSCFST stub columns. Engineering Structures, 2021, 237: 112193
19. Li N, Lu Y, Li S, Gao D. Axial compressive behaviour of steel fibre reinforced self-stressing and self-compacting concrete-filled steel tube columns. Engineering Structures, 2020, 222: 111108
20. Liu Z, Huang D, Li N, Lu Y. Mechanical behavior of steel-fiber-reinforced self-stressing concrete filled steel tube columns subjected to eccentric loading. Structures, 2022, 45: 932–950
21. Zeng J, Wang J, Ouyang Y, Zhuge Y, Liao J, Long Y, Zhou J. Tri-axial compressive behavior of expansive concrete and steel fiber-reinforced expansive concrete. Journal of Building Engineering, 2023, 68: 106026
22. Xiong Z, Mai G, Pan Z, Chen Z, Jian J, Wang D, Ling Z, Li L. Synergistic effect of expansive agents and glass fibres on fatigue bending performance of seawater sea sand concrete. Construction and Building Materials, 2024, 421: 135665
23. Chen Z, Yu J, Nong Y, Yang Y, Zhang H, Tang Y. Beyond time: Enhancing corrosion resistance of geopolymer concrete and BFRP bars in seawater. Composite Structures, 2023, 322: 117439
24. Xu L, Pan J, Yang X. Mechanical performance of self-stressing CFST columns under uniaxial compression. Journal of Building Engineering, 2021, 44: 103366
25. Li H, Wang Y, Wang Y, Liu J, Tian Q. Effect of CaO and MgO based expansive agent on deformation and mechanical properties of concrete-filled steel tubes. Construction and Building Materials, 2020, 250: 118723
26. Feng J, Miao M, Yan P. The effect of curing temperature on the properties of shrinkage-compensated binder. Science China Technological Sciences, 2011, 54(7): 1715–1721
27. Zhang G, Li G. Effects of mineral admixtures and additional gypsum on the expansion performance of sulphoaluminate expansive agent at simulation of mass concrete environment. Construction and Building Materials, 2016, 113: 970–978
28. Hou W, Yang J, Zhang Z, Yuan X. Experimental study and application of manufactured sand self-compacting concrete in concrete-filled-steel-tube arch bridge: A case study. Case Studies in Construction Materials, 2021, 15: e00718
29. Chen Z, Gao F, Hu J, Liang H, Huang S. Creep and shrinkage monitoring and modelling of CFST columns in a super high-rise under-construction building. Journal of Building Engineering, 2023, 76: 107282
30. Han X, Han B, Xie H, Yan W, Ma Q. Experimental and numerical study on the in-plane behaviour of concrete-filled steel tubular arches with long-term effects. Thin-walled Structures, 2021, 169: 108507
31. Wang F, Zhao H. Experimental investigation on blast furnace slag aggregate concrete filled double skin tubular (CFDST) stub columns under sustained loading. Structures, 2020, 27: 352–360
32. Younas S, Hamed E, Uy B. Effect of creep on the strength of high strength concrete-filled steel tubes. Journal of Constructional Steel Research, 2023, 201: 107719
33. Jiao Y, Han B, Xie H, Zhu L, Zhou L. Early-age creep behavior of concrete-filled steel tubular members subjected to axial compression. Journal of Constructional Steel Research, 2020, 166: 105939
34. Wang Y, Geng Y, Zhao M, Chen J. Non-linear creep modelling on circular concrete-filled steel tubular columns. Journal of Constructional Steel Research, 2019, 159: 270–282
35. Guo Y, Zhang H, Geng Y, Wang Y. Time-dependent modelling of steel-tube confined concrete columns considering confining and bonding effects. Journal of Constructional Steel Research, 2022, 198: 107577
36. Wang Y Y, Geng Y, Chen J, Zhao M Z. Testing and analysis on nonlinear creep behaviour of concrete-filled steel tubes with circular cross-section. Engineering Structures, 2019, 185: 26–46
37. Neville A M, Dilger W H, Brooks J J. Creep of Plain and Structural Concrete. London: Construction Press, 1983
38. Arutyunyan N K. Some Problems in the Theory of Creep. London: Pergamon Press, 1966
39. Raupov C, Karimova A, Zokirov F, Khakimova Y. Experimental and theoretical assessment of the long-term strength of lightweight concrete and its components under compression and tension, taking into account the macrostructure of the material. E3S Web of Conferences, 2021, 264: 02024
40. Kaminsky A A. Mechanics of the delayed fracture of viscoelastic bodies with cracks: Theory and experiment. International Applied Mechanics, 2014, 50(5): 485–548
41. Yang Z, Zhu H, Zhang B, Dong Z, Wu P. Short-term creep behaviors of seawater sea-sand coral aggregate concrete: An experimental study with rheological model and neural network. Construction and Building Materials, 2023, 363: 129786
42. Binder E, Königsberger M, Díaz Flores R, Mang H A, Hellmich C, Pichler B L A. Thermally activated viscoelasticity of cement paste: Minute-long creep tests and micromechanical link to molecular properties. Cement and Concrete Research, 2023, 163: 107014
43. Gan Y, Vandamme M, Chen Y, Schlangen E, van Breugel K, Šavija B. Experimental investigation of the short-term creep recovery of hardened cement paste at micrometre length scale. Cement and Concrete Research, 2021, 149: 106562
44. Li Y, Ke L, Li C, Feng P, Feng Z, Qiu M. Retardation mechanisms and modeling of fatigue crack growth of a high-strength steel after single overload. International Journal of Fatigue, 2024, 183: 108267
45. Oppong F, Yao N, Zhang W, Liu Y, Kolawole O. Tentative application of expansive cementitious materials in grouting—A systematic review. Case Studies in Construction Materials, 2023, 18: e02113
46. Guo J, Zhang S, Qi C, Cheng L, Yang L. Effect of calcium sulfoaluminate and MgO expansive agent on the mechanical strength and crack resistance of concrete. Construction and Building Materials, 2021, 299: 123833
47. Lai M H, Binhowimal S A M, Griffith A M, Hanzic L, Wang Q, Chen Z, Ho J C M. Shrinkage design model of concrete incorporating wet packing density. Construction and Building

Materials, 2021, 280: 122448
48. Tang S, Huang D, He Z. A review of autogenous shrinkage models of concrete. Journal of Building Engineering, 2021, 44: 103412
49. Nguyen Q D, Afroz S, Zhang Y, Kim T, Li W, Castel A. Autogenous and total shrinkage of limestone calcined clay cement (LC3) concretes. Construction and Building Materials, 2022, 314: 125720
50. Zhang J. Recent advance of MgO expansive agent in cement and concrete. Journal of Building Engineering, 2022, 45: 103633
51. Li B, Wu C, Li Y, Wang S, Jia L, Xia D. Expansive behavior of high-strength self-stressing and self-compacting concrete: Experimental study and analytical model. Construction and Building Materials, 2022, 353: 129080
52. Menetrey P, Willam K J. Triaxial failure criterion for concrete and its generalization. ACI Structural Journal, 1995, 92(3): 311–318
53. Lee Y, Kim J. Numerical analysis of the early age behavior of concrete structures with a hydration based microplane model. Computers and Structures, 2009, 87(17–18): 1085–1101
54. Chu I, Kwon S H, Amin M N, Kim J. Estimation of temperature effects on autogenous shrinkage of concrete by a new prediction model. Construction and Building Materials, 2012, 35: 171–182
55. Thomas J J, Musso S, Prestini I. Kinetics and activation energy of magnesium oxide hydration. Journal of the American Ceramic Society, 2014, 97(1): 275–282
56. Mo L, Fang J, Hou W, Ji X, Yang J, Fan T, Wang H. Synergetic effects of curing temperature and hydration reactivity of MgO expansive agents on their hydration and expansion behaviours in cement pastes. Construction and Building Materials, 2019, 207: 206–217